NTNU

Norwegian University of
Science and Technology

# Path sampling study of proton transfer reactions using coupled cluster based molecular dynamics

Ola Aarøen

Chemistry
Submission date: May 2016
Supervisor: Titus van Erp, IKJ

Norwegian University of Science and Technology
Department of Chemistry

**Abstract**

Path sampling techniques have been shown to be very efficient tools to study rare events in chemical reaction simulations. Sampling techniques are useful when looking at fairly simple reactions as the breaking of a bond in a single Hydrogen molecule, at the denaturation of DNA molecules or the formation of zeolites – implementing specialized force fields, electron density functionals or ab initio wave function theory. Electron correlation methods, however, are not as widespread in use when it comes to molecular simulations. They scale very badly with increasing system size and basis set, and they are thus very expensive for the gain in accuracy they provide. They require much more computational resources and time than cheaper methods like density functional theory, a method that is well established in molecular dynamics and sampling studies.

But since electron correlation methods are the most accurate at describing the electronic system, this work attempts to join the advantages of a dynamics algorithm preforming transition interface sampling with coupled-cluster calculations from an external quantum chemistry program. The system studied was the proton transfer reaction in the protonated water-trimer, a relatively small system and simple reaction, which has been studied previously with specialized potentials, density functionals, and perturbation theory.

This work contains the first calculation of the reaction rate, using transition interface sampling simulations on the catalyzed proton transfer reaction in the protonated water-trimer. Also included in this work is the first attempt to harvest reactive pathways using coupled-cluster based molecular dynamics.

Using both a TIS and a RETIS scheme, we calculated a rate of reaction for the catalyzed proton transfer in the protonated water trimer. We also generated two trajectories using the coupled-cluster interface with dynamics, which gave us a reactive pathway for the system.

**Sammendrag**

Teknikker basert på path sampling har vist seg å være veldig effektive verktøy i studier av såkalte *rare events* i kjemiske reaksjoner. Fra å se på forsåvidt enkle reaksjoner som å bryte bindingene i ett hydrogenmolekyl, til denaturering av DNA eller formasjon av zeolittstrukturer - ved hjelp av spesialiserte potensialer, elektron funksjonaler eller *ab initio* bølgefunksjonsteori.

Elektronkorrelasjonsmetoder derimot er ikke like mye brukt i molekylmodellering. De skalerer dårlig med økende system og antall basisfunksjoner, og er derfor veldig dyre teknikker for den økte nøyaktigheten de tilbyr. De krever mye mer beregningsressurser og -tid enn funksjonalteori, en metode som er mye brukt i molekyldynamikk og path sampling.

Siden elektronkorrelasjon er å regne som meget nøyaktig når det gjelder beskrivelse av et elektronsystem, skal vi iløpet av dette arbeidet forsøke å kombinere en dynamikkalgoritme med coupled-cluster beregninger fra ett eksternt program. Systemet som ble undersøkt, var den protonerte vann-trimeren, ett relativt simpelt system og enkel reaksjon, som har vært studert nøye tidligere med spesialiserte potensialer og perturbasjonteori.

I dette arbeidet presenteres en reaksjonsrate for den katalyserte protontransportsreaksjonen i vann-trimersystemet, beregnet ved bruk av transition interface sampling. I tillegg er det også gjort forsøk på å generere reaktive baner ved bruk av coupled-cluster basert dynamikk.

Vi beregnet reaksjonsraten i den katalyserte protontransportsreaksjonen med både TIS og RETIS algoritmer. Vi klarte også å generere to baner med coupled-cluster-dynamikk, som gav oss en reaktiv bane for systemet.

**Acknowledgements**

The work during this thesis was carried out under the supervision of Associate Professor Titus van Erp and the co-supervision Professor Henrik Koch, both at the department of chemistry. Firstly, I would like to thank Titus van Erp for giving me the opportunity to work with this thesis, and for all the help and guidance he has provided throughout these last two years. I would also like to thank Henrik Koch for the guidance provided on quantum chemistry, electron correlation, and help using the quantum chemical programs QChem and CFour.

Thanks also go to Enrico Riccardi, Anders Leirvik, Rolf Heilemann Myhre and Eirik Hjertenæs – for helping me understand the theory behind the code, and for guiding me on the coding itself. Many thanks also to Ole Edvard Kristensen, for proof-reading my thesis before submission. And thanks to Christopher Dellago for providing us with the source code of his work with the Stillinger-David potential.

And lastly, but not forgotten, I want to thank my class; Nora, Karen, Linda, Anh and Filip – for every moment that made the last 5 years unforgettable.

# Contents

# Chapter 1

# Introduction

In the world of chemistry one of the simplest, yet most interresting substances we know is water. It is often described as the prerequisite of life in the universe, in our enviroment it exist naturally in three phases: solid, liquid and gas. Water has a characteristic structure due to the two lone pairs on oxygen that form hydrogen bonds, which gives it many of its nice properties like hydrogen bonding in liquid and solid state, its strong solubility of polar and ionic compounds, and let us not forget its "Mickey Mouse shape".

There is a wide variety of classical force fields that model water, which have been highly successful in reproducing experimental radial distribution functions, vibrational spectra, and phase diagrams [1–4]. However, almost all of these force fields do not allow for the breaking of chemical bonds or the description of the hydronium ion, $(H_3O)^+$. The Stillinger-David potential[5] is one of the few potential that have been developed for the study of proton transfer reactions in water with reasonably success.

The potential models a water molecule as three electric charges for the three atoms, and a polarizable oxygen atom. The polarization model of water by Stillinger and David has proven to be quite effective at both describing the formation of hydrogen bonds in water, and when including the molecular interaction and the charge interaction inside a water molecule, the calculation of e.g. vibrational spectra[6] and cluster formation[7] becomes possible. The model also gives results that agree with experimental values for the dipole moment of a water molecule [8],

and has been used to study proton transfer in water systems [9].

We chose to study the proton transfer of the protonated water trimer specifically, since this is reaction in a system which has been studied thouroughly with a wide combination of reaction techniques and models for the systems energy. Geissler et al. [9] used the Stillinger-David potential with the Transition Path Sampling method to study the reactive pathways, and later Transition State theory was combined with Density Functional Theory by Geissler et al. [10] to improve on the results with an *ab initio* electronic structure calculation. The potential energy landscape of the reaction pathway was also done with Møller-Plesset Perturbation theory by Geissler et al. [11], comparing the wavefunction-based pertubation theory with that of the density functional theory.

Our study of the system will be testing both the Stillinger-David potential and the Coupled-cluster approximation, combined with a Transition Interface Sampling scheme with replica exhange implemented by van Erp [12], and classical MD. Our results should be comparable with those of Geissler et al., and we can test the concept of using coupled-cluster based path sampling on rare events, as this has never been done before.

# Chapter 2

# Theory

This chapter will focus on the theory behind the calculations preformed in the simulations. First on molecular quantum mechanics and the polarizable Stillinger-David potential that model the water trimer, then the consept or rare events, and the different transition and sampling theories used to calculate a rate of reaction.

## 2.1 Molecular quantum mechanics

In computational quantum chemistry the primary goal is to solve for solutions of the time-independent Schrödinger equation, to determine the systems electronic structure. Central to quantum chemstry is the Born-Oppenheimer approximation, which simplifies both the Hamilton operator and the wave function by neglecting the kinetic energy of the nucleii. Due to their relatively massive size when compared with the electrons, the nucleii are assumed stationary and the repulsion between them constant. What remains of the Schrödinger equation are called the electronic Hamiltonian and the electronic wave function. With the electronic wave function, the solution to the Schrödinger equation is

$$H_{elec}\Psi_{elec} = E_{elec}\Psi_{elec}, \tag{2.1.1}$$

where

$$\Psi_{elec} = \Psi(\vec{r_e}; \vec{R_N}) \quad \text{and} \quad E_{elec} = E_{elec}(\vec{R_N}). \tag{2.1.2}$$

The wave function describes the eletrons motions, depending on the electronic coordinates $\vec{r_e}$ explicitly, and on the fixed nuclear coordinates $\vec{R_N}$ parametically [13, p. 43].

The wave function is supposed to fully describe the system, or with the BO-approximation, the electrons of the system. The *Born interpretation* of the wave function is that the electron(s) described by it will have a probability to be found in the volume $d\tau$ proportional to $|\psi(\vec{r})|^2 d\tau$. Wave functions can be represented by the use of basis functions, or basis sets, and are usually combined to form approximations to orbitals for individual nucleii and molecules in the system.

Solving the Schrödinger equation above becomes an eigenvalue problem, a problem of finding the ground state wave function of a given system with the lowest energy. This usually begins with making a guess of the wave function, and optimizing it by iterating the system *variationally* untill the difference between two steps of the iteration is sufficiently low, described as having achieved a *self-consistent field* (SCF). The variation theory states that

$$E_0 \leq \varepsilon = \frac{\langle \psi_{trial} | \mathcal{H} | \psi_{trial} \rangle}{\langle \psi_{trial} | \psi_{trial} \rangle}, \tag{2.1.3}$$

the system described by the Hamiltonian, $\mathcal{H}$, and the eigenvalue $\varepsilon$ of the trial state $\psi_{trial}$ will always be higher to the eigenvalue of the true ground state of the system, $E_0$, or equal if, and only if, the trial function is identical to the true ground state [14, p. 187].

While this seems like a very straightforward goal to pursue, there are many different methods and ways to achieve this, which all have their advantages and disadvantages.

### 2.1.1 The Hartree-Fock mehtod

What complicates the electronic structure calculation is the fact that there is an electron-electron repulsion energy between every electron in the system. The Hartree-Fock (HF) approximation [13, p. 53–54] to this problem is to have the electronic repulsions be depending on the positions of nucleii (assumed static from BO-approx.) and the average field of the other $N_e - 1$ electrons. It is here assumed that the exact wave function of a system of $N_e$ electrons, $\Psi^0$, is a product of $N_e$

one-electron wave functions $\psi_m^0(\vec{r}_i; \vec{R_N})$, or just $\psi_m^0(i)$, such that:

$$\Psi^0 = \psi_a^0(1) \times \psi_b^0(2) \times ... \times \psi_z^0(N_e). \tag{2.1.4}$$

All one-electron wave functions are on their own solutions to the one-electron equation:

$$h_i \psi_m^0(i) = E_m^0 \psi_m^0(i), \tag{2.1.5}$$

where the one-electron hamiltonian, $h_i = -\frac{1}{2}\nabla_i^2 - \sum_j \frac{Z_j}{r_{ij}}$, operates on electron $i$ in orbital $m$, relative to the other electrons $j$ (charge $Z$ over distance $r$) to give the orbital energy $E_m^0$. The orbital product of $\Psi^0$ does not fulfill the anti-symmetry of the Pauli principle, so the one-electron wave functions are multiplied with a spin-state $\alpha$ or $\beta$ for the states $\uparrow$ and $\downarrow$ (+ and -), respectively [14, p. 227–229].

$$\phi_m^0(\chi_i) = \psi_m^0(i) * \alpha(i) \tag{2.1.6}$$

The spin-orbital $\phi_m^0$ is depending on $\chi_i$, which contains the electrons position and spin. Then the ground state wave function is written as a Slater determinant of the matrix of the $N_e$ spin-orbitals. This gives the wave function anti-symmetry when exchanging electrons.

$$\begin{aligned} \Psi^0(1, ..., N_e) &= \frac{1}{\sqrt{N_e!}} \det \left\{ \begin{array}{ccc} \phi_1(\chi_1) & \dots & \phi_1(\chi_{N_e}) \\ \vdots & \ddots & \vdots \\ \phi_{N_e}(\chi_1) & \dots & \phi_{N_e}(\chi_{N_e}) \end{array} \right\} \\ &\equiv ||\phi_1(\chi_1)\phi_2(\chi_2)\dots\phi_{N_e}(\chi_{N_e})|| \end{aligned} \tag{2.1.7}$$

The normalization factor $\frac{1}{\sqrt{N_e!}}$ is implied in the last line of eq.(2.1.7). The spin-orbitals are iterated over variationally, so that they give the lowest energy from the determinant. But instead of using the Hamiltonian operator, a Fock operator is introduced that operate on the individual orbital wave functions, solving the eigenfunction problem [13, p. 114]

$$f_1\psi_m(1) = \mathcal{E}_m\psi_m$$
$$f_1 = h_1 + \sum_{m'}\{2J_{m'}(1) - K_{m'}(1)\} \tag{2.1.8}$$

where $\epsilon_m$ is the energy of orbital $m$, and $f_1$ is the Fock operator operating on $\psi_m(1)$. The Fock operator is defined by the Coulomb operator $J_m$, which accounts for the Coulombic repulsion between electrons, and the exchange operator $K_m$ which represent the effect of spin correlation to the energy:

$$J_{m'}(1)\psi_m(1) = j_0 \int \psi^*_{m'}(2)\frac{1}{r_{12}}\psi_m(1)\psi_{m'}(2)d\tau_2 \tag{2.1.9}$$
$$K_{m'}(1)\psi_m(1) = j_0 \int \psi^*_{m'}(2)\frac{1}{r_{12}}\psi_{m'}(1)\psi_m(2)d\tau_2 \tag{2.1.10}$$

The Fock operator sums over all occupied orbitals $m'$, and the sum represents the average potential energy of an electron due to the other $N_e - 1$ electrons in the system. The calculation of molecular orbitals can be solved numerically using the Roothaan equations [15], where the differential equation is written as a matrix problem

$$\mathbf{FC} = \mathbf{SC}\epsilon \tag{2.1.11}$$

solving for the expansion coefficients, $\mathbf{C}$, that gives the lowest orbital energies, $\epsilon$, using the overlap of the one-electron orbitals, $\mathbf{S}$, [13, p. 136–138].

This calculation of the orbitals is variational, so it will each iteration find a configuration that is lower in energy than the previous step, until a sufficient minimum difference between two subsequent states.

### 2.1.2 Configuration states and electron correlation energy

The correlation energy is defined as "*the difference between the exact non-relativistic energy of the system $E_0$ and the Hartree-Fock energy ($E_{HF}$) obtained in the limit that the basis set approaches completeness*" Szabo and Ostlund [13, p. 231]

$$E_0 \equiv E_{HF} + E_{corr} \tag{2.1.12}$$

This means that the Hartree-Fock approximation and a *complete* (infinitely large) basis set will only give an upper limit to the true ground state energy, and the correlation energy has a negative value, which when added to this limit gives a result closer to the exact value. An infinitely large basis set is impossible to work with practically, so in calculations one is limited to using a finite set of basis functions.

A finite basis set would give the best possible, lowest in energy, approximation of the ground state wave function $\Psi^0$, but would still lack the correlation energy between the electrons. The HF method with a finite basis set gives a finite number of molecular orbitals, in general an equal number of orbitals to the number of electrons. By ordering the orbitals by lowest energy, and insuring that they are doubly occupied in the lowest half of the orbitals, the result is the ground state wave function of HF. The remaining orbitals, unoccupied, are often refered to as *virtual orbitals*. By including the virtual orbitals in the calculation, and systematically exciting one or more electrons from a previously occupied orbital to a virtual one, the correlation energy can be calculated from the now *multiconfigurational wave function* [13, p. 233]. This is the principle behind the Configuration Interaction (CI) method, where the exact electronic wave function is expressed as a linear combination of all possible excited Slater-determinants from a finite set of spinorbitals from a HF calculation:

$$\Psi = c_0\Psi_0 + \sum_{a,p} c_a^p \Psi_a^p + \sum_{a<b,p<q} c_{ab}^{pq} \Psi_{ab}^{pq} + \dots \tag{2.1.13}$$

where the groundstate $\Psi_0$ is defined as:

$$\Psi_0 = ||\phi_a\phi_b \dots \phi_l\phi_m\phi_n \dots \phi_z||, \tag{2.1.14}$$

so that a singly excited state, where an electron in orbital $m$ is excited to orbital $p$ looks like:

$$\Psi_m^p = ||\phi_a\phi_b \dots \phi_l\phi_n \dots \phi_p \dots \phi_z||. \tag{2.1.15}$$

where an electron from orbital $m$ has been promoted to the orbital $p$.

In eq. (2.1.13) the $c_a^p$ are expasion coefficients of the corresponding excited states and where the summation limits ($a$ sums over occupied orbitals and $p$ over virtual ones, etc.) ensure that unique pairs of spin-orbitals are summmed over in the second sum, uniquie triplets in the third and so on. Thus, any excited determinant of the system will appear only once in the summation in eq. (2.1.13).

Still, to get the exact ground state energy using an infinite set of $N_e$-electron Slater determinants where each determinant itself is constructed using an infitite set of spinorbitals, is impossible. It will also prove to be very computationally demanding to handle even a finite, but still large, set of determinants.

### 2.1.3 The Coupled-Cluster approximation

An important lack of the CI-method discussed above is that the truncated CI (not Full CI) is not size consistent. Size consistency requires that the energy of a simple dimer of two monomers separated by a large distance, should be the same as twice the energy of one monomer of the same dimer [13, p. 261]. One post-HF method that remains size consistent is the Perturbation theory [16], where the correlation energy is calculated size-consitently, but not variationally. This also has it disadvantages, as the energy calculation no longer can be considered an upper bound to the true ground state energy, and may actually appear lower than it.

The Coupled-Cluster approximation (CCA or CC), initially developed in the study of nuclear physics, is a popular *ab initio* method. It is similar to the Perturbation theory in that it is size consistent and not variational, and follows the idea that the correlation is unlikely to arise from interaction with more than one other electron [13, p. 286–289]. Thus, the interaction of simultaneous pair interactions are more important than many-electron interactions. Much like CI-calculations, it defines the exact wave function $\Psi_0$ by the HF-wave funtion, but instead use a *cluster operator*, $C$:

$$\Psi = e^C \Psi_{HF} \tag{2.1.16}$$

where the operator inside the exponential function $e^C$ operates by the series ex-

pansion:

$$e^C = \sum_{i=0} \frac{1}{i!} C^i = 1 + C + \frac{1}{2!} C^2 + \frac{1}{3!} C^3 + ... \tag{2.1.17}$$

The total effect of the cluster operator in this expansion is a sum of all effects of a one-electron excitation operator $C_1$, two-electron operator $C_2$, and so on up to and including $N_e$-electron excitation operator $C_{N_e}$ on the wave function [13, p. 290–291]

$$C = C_1 + C_2 + \ldots + C_{N_e} \tag{2.1.18}$$

and

$$C_1 \Psi_0 = \sum_{a,p} t_a^p \Psi_a^p, \qquad C_2 \Psi_0 = \sum_{a,b,p,q} t_{ab}^{pq} \Psi_{ab}^{pq}, \qquad \ldots \tag{2.1.19}$$

$t_a^p$ is called a single-excitation amplitude, $t_{ab}^{pq}$ a double-excitation amplitude, etc. There is no operator beyond $C_{N_e}$ because $\Psi_0$ has all its electrons in $N_e$ occupied spinorbitals, and there are no more electrons left to excite. In the second quantatization formalism the operators in Equation (2.1.19) can be written as

$$C_1 = \sum_{a,p} t_a^p \hat{c}_p^\dagger \hat{c}_a, \qquad C_2 = \sum_{a,b,p,q} t_{ab}^{pq} \hat{c}_p^\dagger \hat{c}_q^\dagger \hat{c}_b \hat{c}_a, \qquad \ldots \tag{2.1.20}$$

with $\hat{c}^\dagger$ and $\hat{c}$ the creation and annihilation operator, respetively: $\hat{c}_p^\dagger |0\rangle = |p\rangle$ and $\hat{c}_a |a\rangle = |0\rangle$. The excitation coefficients $t_a^p$ are solved iteratively, like the orbital coefficients of the HF method.

The problem regarding computational costs of using huge numbers of excited determinants is also relevant in CC-calculations, and it is therefore common to truncate the cluster operator (eq. 2.1.18) in the expansion so that only certain terms are included in the calculation. The exponential operator is then approximated in many different ways by using for instance just double excitations (CCD), where the cluster operator is approximated by $C \approx C_2$, or when using both singles and doubles (CCSD) approximated by $C \approx C_1 + C_2$, and so on. Still, CCD and CCSD are both very computationally demanding, and scales $N^6$ and $N^7$, respectively, with $N$ basis sets.

## 2.2 The Stillinger-David Potential

The Stillinger-David model defines the function for the potential energy of interaction as consisting of two terms, one with pair-interactions and one with dipole polarizability.

$$\Phi_{total} = \Phi_1 + \Phi_2 \tag{2.2.1}$$

$$\Phi_1 = \sum_{i<j=1}^{N_H} \phi_{HH}(r_{ij}) + \sum_{i=1}^{N_H}\sum_{j=1}^{N_O} \phi_{OH}(r_{ij}) + \sum_{i<j=1}^{N_O} \phi_{OO}(r_{ij}) \tag{2.2.2}$$

The first term calculates the sum of Coulombic forces between each pair of the atoms in the system, with special potential functions for each of the possible atom-atom combinations considered. Since hydrogen in this model can be considered as a lone proton with a point-charge, the potential is chosen so that

$$\phi_{HH}(r) = e^2/r \tag{2.2.3}$$

Is this case the value of $e$ is a product of the atomic charge ($+1$ for hydrogen and $-2$ for oxygen) and a chosen factor so that the square value will give the repulsive/attractive energy between two given particles with the correct energy unit (kcal/mole). An illustration of the potential is shown in Figure 2.1(a)

This relation is also true for the other two pair-potentials. With oxygen-hydrogen and oxygen-oxygen, respectively, behaving at large distances ($r \to \infty$):

$$\phi_{OH}(r) \approx -2e^2/r \tag{2.2.4}$$

$$\phi_{OO}(r) \approx 4e^2/r \tag{2.2.5}$$

and this again is due to the atomic charge of oxygen particles being $-2$, and $+1$ for hydrogen particles. However, unlike with hydrogen, oxygen atoms have (in this model) a full shell of electrons that will result in a deviation from the purely Coulombic form at smaller values of $r$. More specifically, $\phi_{OH}(r)$ will have a energy well, which promotes covalent bond formation between oxygen and hydrogen, see

Figure 2.1(b). The oxygen-oxygen function $\phi_{OO}(r)$ will exhibit repulsion from the overlapping electron clouds that extend from each particle, Figure 2.1(c).

With conditions distance in Angstrom [Å] and energy in kcal/mole, the value of $e$ is chosen as 18.2255287989 (from the source code of Geissler et al. [9]), which gives the squared value of 332.1669. The three potentials are defined in equations 2.2.6-2.2.8,

$$\phi_{HH}(r) = \frac{332.1669}{r} \tag{2.2.6}$$

$$\begin{aligned}\phi_{OH}(r) = &\frac{332.1669}{r}[10 \times e^{-3.69939282r} - 2] \\ &+ [-184.6966743(r - r_e) + 123.9762188(r - r_e)^2]e^{-8(r-r_e)^2}\end{aligned} \tag{2.2.7}$$

$$\phi_{OO}(r) = \frac{1328.6676}{r} + \frac{24}{1 + \exp[2.5(r - 2.90)]} + \frac{90}{1 + \exp[8(r - 2.45)]} + e^{-6(r-2.70)} \tag{2.2.8}$$

With $e^2 = 332.1669$ equations 2.2.3 and 2.2.6 for H-H interaction match, the bonding behavior of 2.2.4 is also quite apparent from the potential energy well in Figure 2.1(b)

It is worth noting that the Stillinger-David model has been modified since its first implementation, and usually with those modifications the parameters of $\phi_{OO}$ and $\phi_{OH}$ are changed somewhat[7] or an almost completely new model is devised[17, 18] In the work done in this thesis however, the functions are implemented as they are defined above.

The second term of the potential becomes a bit harder, as it calculates the dipole moment from the electric field at each particle due to the other particles. The potential has a relatively simple form:

$$\Phi_2 = \sum_{i=1}^{N_o} \sum_{\substack{j=1, \\ j \neq i}}^{N_{tot}} \frac{1}{2} \frac{e_j(\vec{\mu}_i \cdot \vec{r}_{ij})}{r_{ij}^3}(1 - L_O(r_{ij})) \tag{2.2.9}$$

Firstly, the potential sums over all oxygens, and all the neighbours of those oxy-

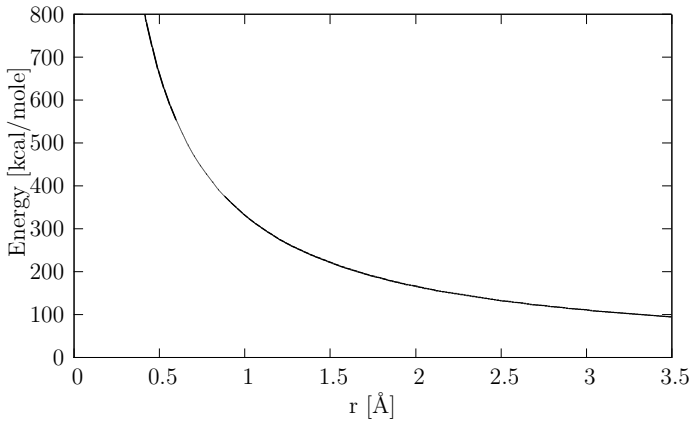


(a) The hydrogen-hydrogen potential $\phi_{HH}$

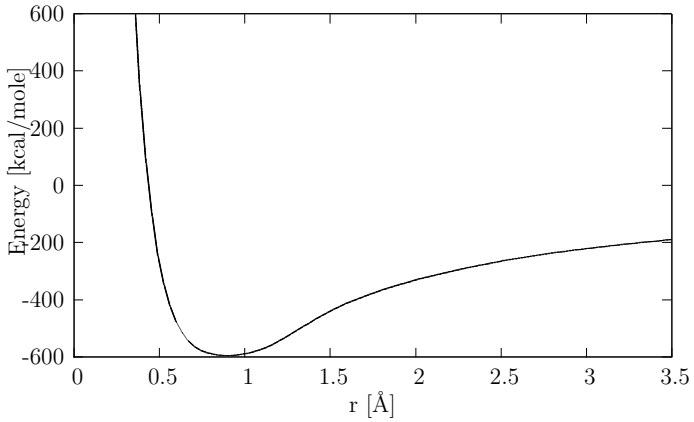


(b) The oxygen-hydrogen potential $\phi_{OH}$

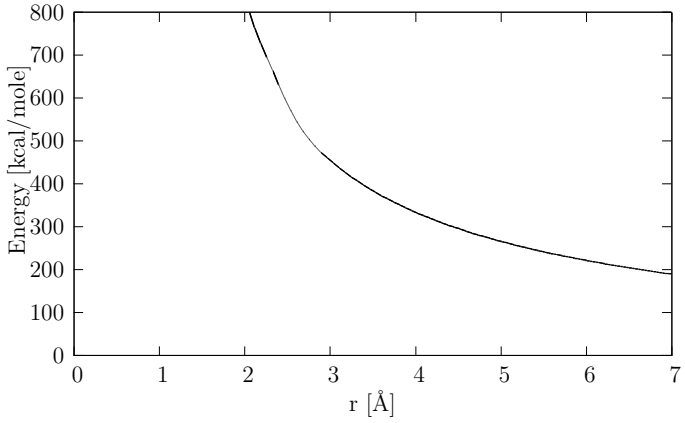


(c) The oxygen-oxygen potential $\phi_{OO}$

**Figure 2.1:** Illustration of the three different pair-potentials. Respectively, (a) eq. 2.2.6, (b) eq. 2.2.7 and (c) eq. 2.2.8

gens, and we again have the protonic charge and energy factor $e_j$. Secondly the potential includes a screening function $(1 - L_O(r))$, which will be defined later. Thirdly the potential includes the polarizable dipole moment on each of the oxygen particles $\vec{\mu}_i$ ($\{xyz\}$-format), calculated from an electric field at that given particle due to neighbouring charges from all other particles in the system. $\vec{r}_{ij}$ is the vector between particles $i$ and $j$ in $\{xyz\}$-format.

The dipole moments $\vec{\mu}_i$ in eq.(2.2.9) are calculated iteratively, using a self-consistent method. An initial guess of the dipole/electric field is construced, using the position of each neighbouring particle in the system, its charge and polarizability.

$$\vec{\mu}_i^{(0)} = \sum_{\substack{j=1,\\ j\neq i}}^{N_{tot}} -\alpha \times e_j \times \frac{1 - K_O(r_{ij})}{r_{ij}^3} \times \vec{r}_{ij} \tag{2.2.10}$$

Each oxygen in this model is regarded as a doubly charged anion $O^{2-}$, with a polarizability, $\alpha$, of $1.444\text{Å}^3$. This value is assigned to model the undissociated water molecules that are most represented, and was chosen by Stillinger and David based on then recent water vapor-phase measurements [8]. A second screening function, $(1 - K_O(r))$, is introduced here. This function will also be defined in a moment.

The dipoles are then iterated, using a tensor which was also created with the initial guess, the required number of times until the difference between dipoles at each iteration step converge within a given tolerance ($10^{-18}$).

$$\vec{\mu}_i^{(n+1)} = \sum_{\substack{j=1,\\ j\neq i}}^{N_o} \mathbf{A}_{ij} \cdot \vec{\mu}(i)^{(n)} \tag{2.2.11}$$

The tensor $\mathbf{A}_{ij}$ is a $(3 \times 3)$-matrix for each oxygen-oxygen pair, construced once for the given geometry of the system at the time, by the following equation:

$$\mathbf{A}_{ij}^{(3\times3)} = \frac{3times(1 - K_O(r_{ij}))}{r_{ij}^5} times(\vec{r}_{ij} \cdot \vec{r}_{ij}^T)^{(3\times3)} - \frac{1 - K_O(r_{ij})}{r_{ij}^3} times\mathbf{I}^{(3imes3)} \tag{2.2.12}$$

where $\mathbf{I}$ is the $(3\times3)$ identity matrix, and $(\vec{r}_{ij}\cdot\vec{r}_{ij}^T)^{(3\times3)}$ is a matrix with cross-terms

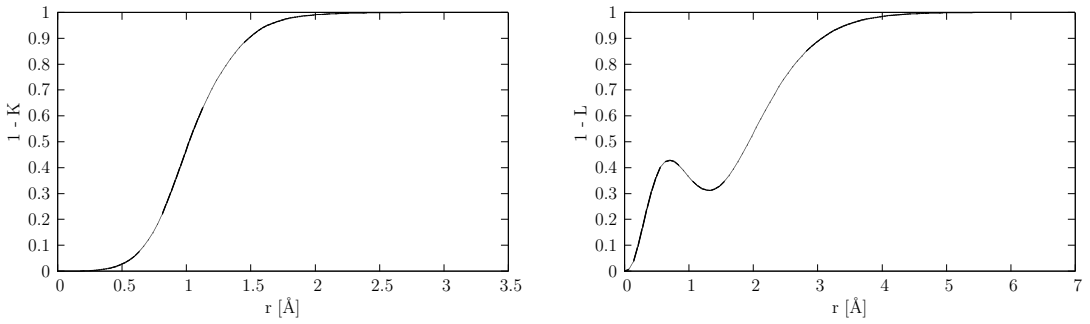


(a) Polarization response function, $1 - K$ (b) Polarization interaction function, $1 - L$

**Figure 2.2:** The two polarization functions, $1 - K$ (a) and $1 - L$ (b), equations (2.2.13) and (2.2.14), respectively. Used in the calculation of polarizable dipoles in equations (2.2.9) and (2.2.10).

of the vector between the particles $i$ and $j$.

There is also a second use of the previously mentioned screening function $(1 - K_O(r))$. Both of these functions are related to the behavior of the oxygen atoms in the model, and serve to modify the potential energy at close distances, see Figure 2.2.2(a) and 2.2.2(b). In the case of more separated atoms, both of the functions will converge to 1 - thus reducing the interation to conventional electrostatics, using only the first term of the total potential $\Phi$. The choice of writing them as $1 - L$ and $1 - K$ as supposed to just $L$ and $K$ is done only to further signify this converging behavior. Also, since the hydrogen particles in this model are assumed to be without without electrons, the values of $L$ and $K$ will always be zero in the case of H-O or H-H pairs, for all values of $r$. Thus, the subscript $O$ in both functions can be dropped from now on.

With all the same conditions as mentioned before, $r$ the distance between particles in Ångstrom and $r_e$ the equilibrium distance of the O-H bond, the screening functions $K$ and $L$ have the following form.

$$1 - K(r) = \frac{r^3}{r^3 + 1.855785223(r - r_e)^2 \times e^{-8(r-r_e)^2} + 16.95145727 \times e^{-2.702563425r}} \tag{2.2.13}$$

$$1 - L(r) = 1 - e^{-3.169888166r} \times$$
$$(1 + 3.169888166r + 5.024095492r^2 - 17.99599078r^3 + 23.92285000r^4) \quad (2.2.14)$$

Here $e$ is the natural exponential function, and not the charge factor.

The chosen parameters in both polarization functions have also been modified over time, but unlike the potential functions (2.2.6-2.2.8) not until the introduction of the Stillinger-Weber model [17]. For the definitions of pair-potential forces and polarization forces from dipole moments, see Appendix A.

## 2.3 Rare Events simulation

With the use of conventional Molecular dynamics (MD) one is able to compute many structural and conformational properties of a system, while there are many dynamical phenomena that are impossible to be studied this way. Specifically, conventional MD cannot be used to study an activated process – that is, dynamics that a involve step which is considered a *rare event*. This rare event in chemical reaction simulations is usually the crossing of a high energy barrier between stable states which, by using conventional MD, might have an extremely low probability to occur. Reactions like protein folding, formation of clusters and diffusion of gas molecules in solids are basically impossible to model with a brute-force MD, because of this bottleneck in the potential energy surface in phase space that the system must happen upon by chance to overcome.

In the unlikely case that the rare event actually happens during a simulation, it will in most cases progress quickly enough to be simulated within the time scale of MD (in the nano second to pico second scale)[19, p. 431-432]. Therefore, it is preferable to have methods of avoiding the needless wandering around in either reactant state, and rather enhance the probability of observing a rare event.

## 2.4 Transition State theory

A method to simulate how chemical reactions happen, deviced by Wigner and Eyring, is called the Trasition State Theory (TST) [20]. The theory states that for a reversible reaction

$$\mathrm{A} \rightleftharpoons \mathrm{B} \tag{2.4.1}$$

where A and B are the two stable states, respectively the reactant state and the product state, the reactants must have a sufficient kinetic energy to overcome the potential energy barrier that exist inbetween the states A and B. The height of the barrier from the reactant state is the activation energy for that specific reaction, and at the peak of the barrier the theory imagines the Transition State (TS) of the system. At this state, the reactants have created an unstable complex state with high potential energy, that can either dissociate through into the product state or back to the reactant state. By imagining the following reaction for the two states A and B in eq.(2.4.1)

$$\mathrm{A{-}H} + \mathrm{B} \rightleftharpoons \mathrm{A} + \mathrm{H{-}B}, \tag{2.4.2}$$

where a bond between A and H is broken, and the hydrogen binds to another atom B. Then the theorized and highly unstable transition state of the system will be

$$\mathrm{A{\cdots}H{\cdots}B}, \tag{2.4.3}$$

with the hydrogen simultaneously bonded to both A and B. The potential energy barrier between the two stable states, and the transition state are all illustrated in Figure 2.3 below.

The reaction rate $k$ of such a reaction is defined by Arrhenius' law as

$$k = A \cdot e^{-E_a \beta} \tag{2.4.4}$$

where $E_a$ is the activation energy of the reaction, $\beta$ is defined as $\frac{1}{\mathrm{RT}}$, with R the universal gas constant and T temperature in Kelvin, $A$ is here a frequency factor. The rate constant has units $\frac{1}{s}$, and represents the number of bonds that are broken

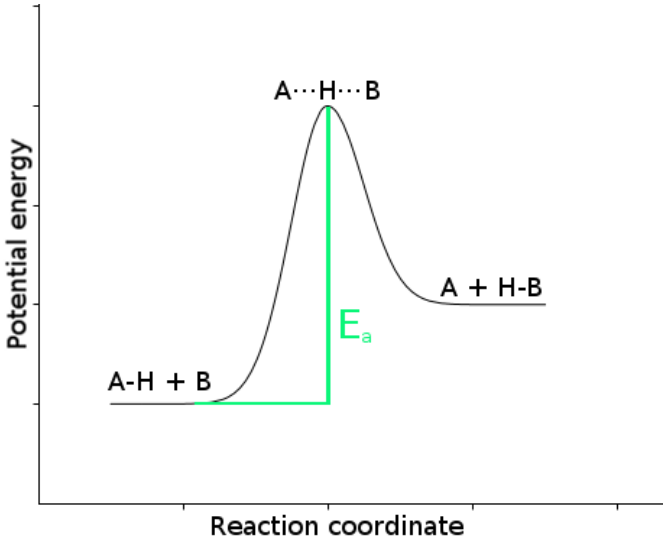


**Figure 2.3:** The transition state in eq.(2.4.3), between reactant state to the left and product state to the right, with the activation energy barrier $E_a$. The reaction coordinate is a coordinate that describes the progress of the reaction. By the reaction from 2.4.3, the reaction coordinate could for instance be the distance from A to H.

between A and H per units of time.

TST has its limitations when considering more complex systems, where the transition state no longer can be thought of as a single point on the potential energy surface, but rather a multidimensional surface in the free energy landscape. When the free energy difference between reactant state and the TS surface is used in the TST equation, the free energy barrier also is limited by the degrees of freedom used to describe the free energy surface [21].

TST also assumes a simple and short trajectory across the energy landscape, crossing the TS surface only once from $A$ to $B$ when in reality it could follow a trajectory or path, that have many crossings back and forth before settling in either stable states.

## 2.5 Path Sampling techniques

Instead of focusing on the transition of a system as the crossing of a specific point or plane in a multi-dimensional landscape, it can be more favorable to think of the transition of a reaction as a trajectory or path of least resistance between the stable states A and B. Doing so, we do not need any information about the system outside of these two defined states, being the reactant state and product state. This is achieved by assuming that a simple order parameter can be defined, that easily differentiate A and B states, and using this parameter to specify if the system at any given time is within the area that defines either of these states. This method of simulation is called Transition Path Sampling (TPS), as it focuses on finding multiple possible pathways through the free energy landscape with a Monte Carlo approach, not limited to crossing one defined point or surface. [22] By connecting the two states with a trajectory or path, we can then by different methods explore all likely transition pathways, collectively called a Path Ensemble, and analyze them to find the transition mechanism for the reaction.

A trajectory or path is often defined as a sequence of states, like an ordered collection of still frames taken of the system along the path. In a path of length $\mathcal{T}$, frames or states are seperated in time by a small increment $\Delta t$

$$x(\mathcal{T}) \equiv \{x_0, x_{\Delta t}, x_{2\Delta t}, ..., x_{\mathcal{T}}\} \tag{2.5.1}$$

where for a molecular system evolving with Newton's equation of motion or Langevin dynamics, the state $x_{i\Delta t}(r, p)$ is a complete representation of the system at time $i$, with both positions $r$ and momentum $p$ of every particle in the system. The states in the path can also be refered to as *time slices*, as they are discrete slices in time of a continuous path see Figure 2.4.

Not every path imaginable is realistic to consider when trying to simulate a rare event. In general, the probalitity to move to a time slice $x_{t+\Delta t}$ depends only on the last state in the path, $x_t$, and the specific dynamics that are applied in the simulation. Thus, the total probability density of a path can be defined as a product of all the single time step probabilties $p(x_t \to x_{t+\Delta t})$ and the probability distribution of the initial condition, see Figure 2.4.

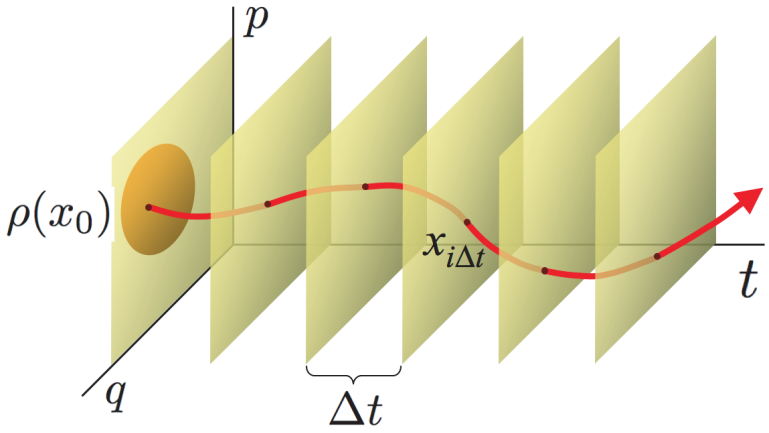


**Figure 2.4:** A trajectory $x(\mathcal{T})$ dicretized into time slices, seperated by a time increment $\Delta t$. The slice shown, $x_{i\Delta t}$, is a complete description of the system at the time $i\Delta t$. In the case of Newtonian and Langevin dynamics, this means that each slice includes both positions and momenta of all particles. Also the initial conditions for the trajectory $\rho(x_0)$, see eq (2.5.2). Figure taken from article of Dellago et al. [23, p. 354]

$$\mathcal{P}[x(\mathcal{T})] = \rho(x_0) \prod_{i=0}^{\mathcal{T}/(\Delta t)} p(x_t \to x_{t+\Delta t}). \tag{2.5.2}$$

With the distribution of the initial conditions $\rho(x_0)$ being dependant on either energy $E$ or temperature. Using the either the *canonical* distribution (with defined temperature, $\beta = 1/k_B T$)

$$\rho(x_0) = \frac{\exp[-\beta \mathcal{H}(x_0)]}{\int dx \exp[-\beta \mathcal{H}(x_0)]}, \tag{2.5.3}$$

or *microcanonical* distribution (with defined energy, $E$)

$$\rho(x_0) = \frac{\delta[E - \mathcal{H}(x_0)]}{\int dx \delta[E - \mathcal{H}(x_0)]}. \tag{2.5.4}$$

to get the initial conditions[23]. $\mathcal{H}(x_0)$ is the Hamiltonian of the system at $x_0$, and it propagates the system in time by updating positions from velocities.

Since the focus of the simulation is to model the rare event transition of the system, the path ensemble is restricted to only include reactive paths, i.e. paths

that connect the states A and B. More specifically, only states that have been defined to start within the region A and end in B. The probability of such a reactive path is

$$\mathcal{P}_{AB}[x(\mathcal{T})] = h_A(x_0)P[x(\mathcal{T})]h_B(x_\mathcal{T})/Z_{AB}(\mathcal{T}) \tag{2.5.5}$$

where $h_A$ and $h_b$ are characteristic functions of the system $x$ that define the two regions A and B like so:

$$h_{A,B}(x) = \begin{cases} 1 & \text{if } x \in A, B \\ 0 & \text{if } x \notin A, B \end{cases} \tag{2.5.6}$$

Therefore, a path not beginning in region A and ending in region B will have a zero statistical weight on the result, and a path that fulfills the criteria of these two functions *may* have a non-zero weight. The probability distribution of the reactive pathways are normalized by

$$Z_{AB}(\mathcal{T}) = \int \mathcal{D}x(\mathcal{T})h_A(x_0)\mathcal{P}[x(\mathcal{T})]h_B(x_\mathcal{T}) \tag{2.5.7}$$

$$\int \mathcal{D}x(\mathcal{T}) = \int ... \int dx_0 dx_{\Delta t} dx_{2\Delta t} ... dx_\mathcal{T} \tag{2.5.8}$$

In the case of Newtonian dynamics, the system evolves deterministically in time, which means that the state of the system at time $i\Delta t$ is completely determined by the initial state $x_0$, and each state in time can be defined by the initial state at time $t = 0$ and a propagator $\phi_t(x_0)$. With such deterministic dynamics, the single time step probability in eq (2.5.2) can be written:

$$p(x_t \to x_{t+\Delta t}) = \delta[x_{t+\Delta t} - \phi_{\Delta t}(x_t)], \tag{2.5.9}$$

where $\delta$ is the Dirac delta function. This also changes the reactive path probability (2.5.5) to be given by

$$\mathcal{P}_{AB}[x(\mathcal{T})] = \rho(x_0)h_A(x_0)\prod_{i=0}^{\mathcal{T}/(\Delta t-1)}\delta[x_{i+1} - \phi_{\Delta t}(x_{i\Delta t})]h_B(x_{\mathcal{T}})/Z_{AB}(\mathcal{T}) \quad (2.5.10)$$

with the factor:

$$Z_{AB}(\mathcal{T}) = \int dx_0\rho(x_0)h_A(x_0)h_B(\mathcal{T}) \quad (2.5.11)$$

to normalize the distribution. From the new equations (2.5.10–2.5.11) we can see that all but the initial state of the system have been integrated out, making the initial state integral the only remaining one in the probability density calculation. Thus, only the initial conditions of $x_0$ determine whether a path will reach $B$ or not, as is logically sound for a completely deterministic trajectory.

The initial pathway connecting reactant and product state can be generated by a very long MD simulation; but as mentioned before the likelyhood of a rare event occuring within the time scale is practically zero. With higher temperature there may be a higher probability of getting a transition within a MD simulation but it might be a very different trajectory than a lower temperature one, and a systematic cooling procedure is necessary to bring the system down in temperature by small steps. Another method is to re-implement the use of a reaction coordinate, which can be used to drive the system from A to B, and to obtain an initial path.

The TPS method has been applied to a number of different calculations [24] , including the study of proton transfer in the water trimer[9–11] that will be studied in this work.

### 2.5.1 Shooting moves on the path ensemble

The path ensemble is generated by taking an initial reactive path and by various methods expanding the collection by generating new paths to the ensemble. Generating the initial path, using an orderparameter or reaction coordinate is achieved by doing a number of *shooting moves* from the initial state of the system at time $t = 0$, keeping track of the reaction coordinate, until the criteria that defines stable region B has been reached. Once this inital path connecting A and B is generated, new paths can be found by repeating the shooting move on exisiting time

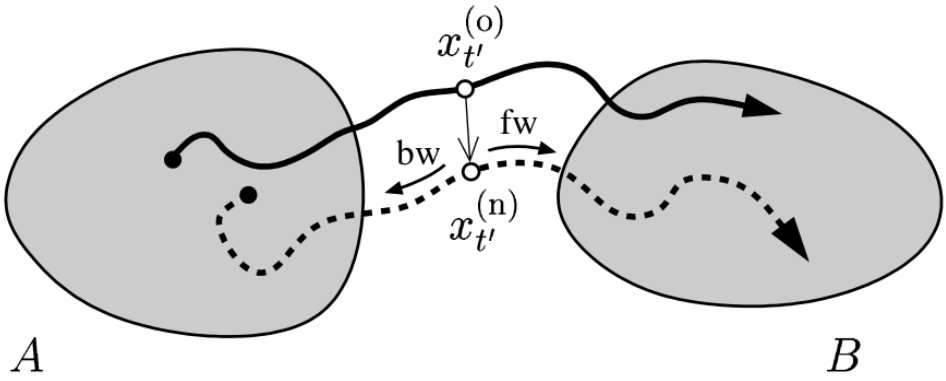


**Figure 2.5:** Illustration of a shooting move. A time slice, $x_{t'}^{(o)}$,at time $t'$ is chosen from the old path (solid line), and the positions are perturbed with $\delta r$ to create a new time slice $x_{t'}^{(n)}$. Then the system is propagated forwards (fw) and backwards (bw) in time to generate the new path (dashed line), connecting regions A and B. Figure taken from article of Dellago et al. [22, p. 17]

slices [23].

A shooting move is preformed by choosing a random time slice of an already existing and reactive path $x_{t'}^{(o)}$, and perturbing for instance the momenta or the positions of the particles in the old time slice, effectively creating a new time slice at the same moment in time different from the old. This new time slice is used to create two new path segments, going forwards and backwards in time, starting from this point.

In deterministic dynamics, choosing a point $x_{t'}^{(o)}$ of an old path and changing the momenta by a small amount $\delta p$, will result in generation of a new path (see Figure 2.6). In stochastic dynamics the randomization of velocities will be the effective shooting move, generating a new path (see Figure 2.5). The new path must also fulfill the criteria of equation (2.5.10): starting in region A and ending in B to have a non-zero weight.

Much like the probability density of observing a path in eq.(2.5.2), the probabilty of generating a forwards and backwards path segment from a shooting point is defined as:

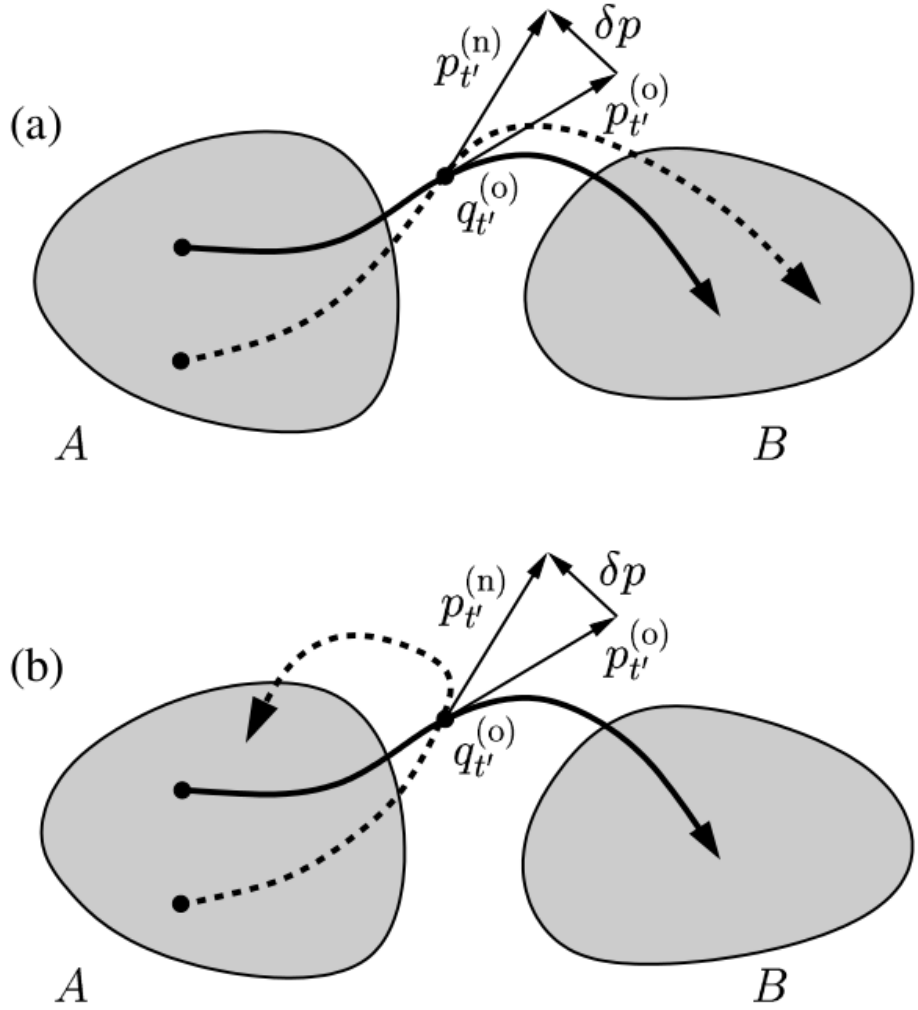


**Figure 2.6:** Illustration of an accepted shooting move (a), and a rejected shooting move (b). The momenta in time slice at time $t'$ of the old path (solid line) are perturbed by adding a random set of momentum values $p_{t'}^{(n)} = p_{t'}^{(o)} + \delta p$. The new path (dashed line) is generated by propagating forwards and backwards in time, and in (a) the system enters region B - making the criteria of a reactive path. Figure taken from article of Dellago et al. [22, p. 22]

$$P^f_{gen}[x^{(o)}(\mathcal{T}) \to x^{(n)}(\mathcal{T})] = \prod_{i=t'/\Delta t}^{\mathcal{T}/(\Delta t-1)} p(x^{(n)}_{i\Delta t} \to x^{(n)}_{(i+1)\Delta t}) \tag{2.5.12}$$

for a segment forwards in time, and

$$P^b_{gen}[x^{(o)}(\mathcal{T}) \to x^{(n)}(\mathcal{T})] = \prod_{i=1}^{t'/\Delta t} \bar{p}(x^{(n)}_{i\Delta t} \to x^{(n)}_{(i-1)\Delta t}) \tag{2.5.13}$$

for a segment backwards in time, with the transition probability of a backwards move in time $\bar{p}(x \to x')$.

Considering the propagation of deterministic dynamics, and scaling the random momenta of the shooting point correctly, the probability of accepting a new path generated from the shooting move can be simplified to [22]

$$P_{acc}[x^{(o)}(\mathcal{T}) \to x^{(n)}(\mathcal{T})] = h_A(x^{(n)}_0)h_B(x^{(n)}_{\mathcal{T}}) \min\left[1, \frac{\rho(x^{(n)}_{t'})}{\rho(x^{(o)}_{t'})}\right] \tag{2.5.14}$$

implying that any new path connecting region A and B is accepted with a probability that depends only on the shooting points of the old and new paths.

The whole process of shooting to generate a new path can be summarized as the following algorithm:

1. A random shooting point $x^{(o)}_{t'}$ at time $t'$ is selected and pertubed with $\delta x$ to create a point in the new pathway $x^{(n)}_{t'}$.

2. This shooting point is accepted if and only if the ratio $\rho(x^{(n)}_{t'})/\rho(x^{(o)}_{t'})$ is bigger than a random number taken from the uniformly distributed interval $[0, 1]$.

3. If the shooting point is accepted, the forwards or backwards segment is grown from the shooting point.

4. If the first segment reaches the required region A or B, backwards or forwards, respectively – the other segment of the path is grown from the shooting point.

If any of the steps 2.–4. are rejected, the process begins from start at 1. by choosing a new shooting point. This process of creating new paths to the path

ensemble is what was imagined by Bolhuis et al. [24] as "*Throwing ropes over rough mountain passes in the dark*", also used as title of their paper.

The transition path ensemble of reactive pathways as in eq. (2.5.10) is now a collection of possible pathways connecting reactant state with product state. Pathways that have been sampled in this ensemble can be analyzed to gain information about the mechanism of the reaction and its rate.

### 2.5.2 Reaction rate calculation

By going back to the notion of eq. (2.4.1), an equilibrium between to states, A and B, the rate of a reaction going from state A to state B can be described as

$$k_{AB} = \lim_{dt \to 0} \frac{1}{dt} \frac{\#\text{ states A that transform into state B within } dt}{\#\text{ states A}}. \tag{2.5.15}$$

The more mathematical way of writing this would be to use the defined regions from equation 2.5.6 in a time correlation function related to the two states [19, p. 451-454]

$$C(t) = \frac{\langle h_A(x_0) h_B(x_t) \rangle}{\langle h_A \rangle} \tag{2.5.16}$$

where $C(t)$ is the time correlation function related to the transition from states A to B, with $x_t$ being the coordinates and velocities of all the particles in the system at a time $t$. The function gives a conditional probability of finding the system within the defined region of B at a given time $t$ in a path, provided that it started within region A at time $t = 0$.

Assuming that the transitions are rare events, the rate constant can be found from the plateu of the time derivative of the correlation function in eq. (2.5.16), see Figure 2.7

$$k(t) = \frac{d}{dt} C(t) = \frac{\langle h_A(x_0) \dot{h}_B(x_t) \rangle}{\langle h_A \rangle} \tag{2.5.17}$$

Since accepted paths *must* either start or end in the region of A, the correlation function can be approximated, to rely on the average of paths that visit region B

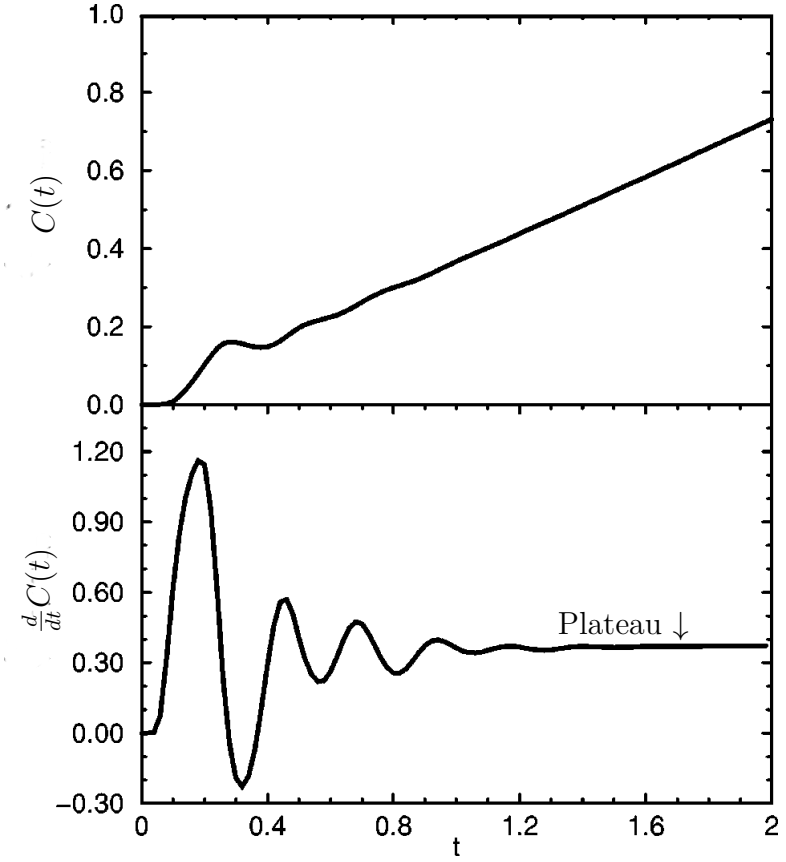


**Figure 2.7:** A TPS correlation function ($C(t)$, Equuation 2.5.16) at the top, and its time-derivative (Equation 2.5.17) at the bottom, showing the plateau that gives the rate constant. Figure modified from article by van Erp et al. [25]

at time $t$ and the time $t$ relative to the reaction time, given by the forwards and backwards rate of the reaction [26]

## 2.6 Transision interface sampling

Transition interface sampling [25] (TIS) is a sampling method based on a calculation of the flux of the reaction. But unlike in TPS, the TIS approach measures the effective positive flux, which implies that only positive transititons beginning in reactant state A and ending in product state B, contribute to the rate calculation. Also, instead of a single dividing surface at approximately the transition state, as in TST, several surfaces, or interfaces, are introduced and the flux is defined based

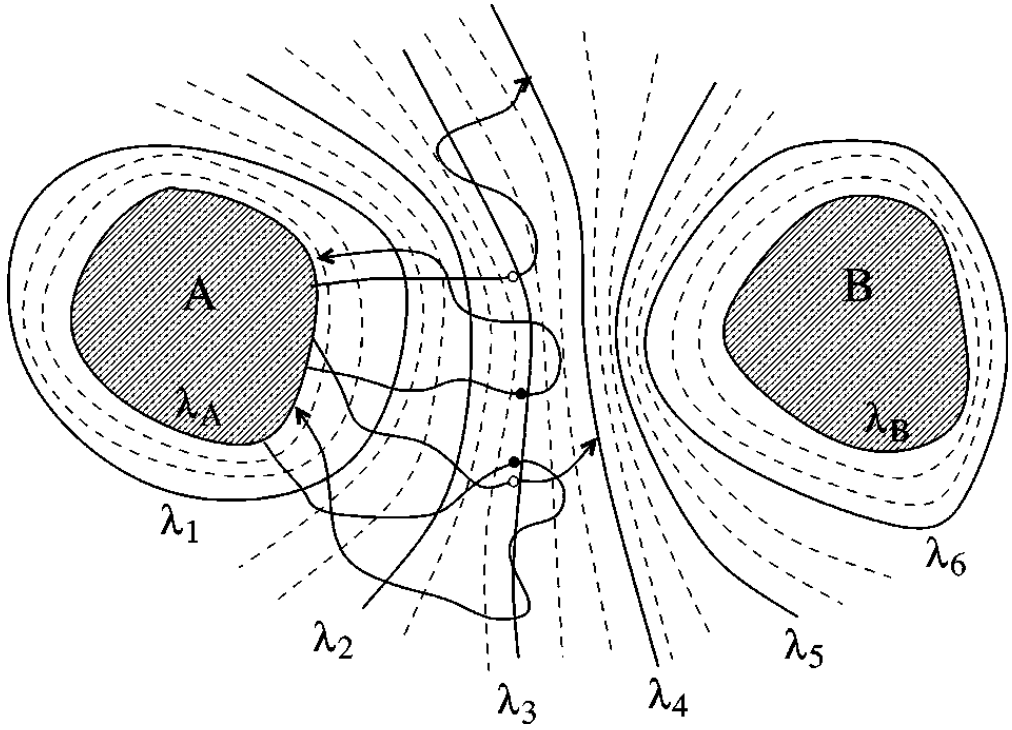


**Figure 2.8:** Illustration of the interfaces separating the stable regions A and B in phase space. The two regions are defined by the respective interfaces $\lambda_A$ and $\lambda_B$, and examples of trial paths starting within region A are shown as the arrow lines that cross the different interfaces $\lambda_1$–$\lambda_6$ in phase space. Figure taken from article of van Erp et al. [25].

on the crossing of these interfaces. The interfaces are separated in phase space by an order parameter or reaction coordinate, $\lambda(x)$, of the system that define the progress of the reaction, see Figure 2.8.

In order to formulate the flux properly, from one state into another, the entire phase space have to be re-defined so that the system is never in an intermediate region, but related to either A or B. This is solved by introducing the *overall states* $\mathcal{A}$ and $\mathcal{B}$. In addition to including phase space points within A and B, state $\mathcal{A}$ also covers states that visit A before reaching B when integrating backwards in time. Similarly, $\mathcal{B}$ covers states that visits region B before A. All of this just means that the characteristic functions used in TST to define the two regions (eq. 2.5.6) can be re-used, only modified to describe the overall states $\mathcal{A}$ and $\mathcal{B}$.

$$h_{\mathcal{A},\mathcal{B}}(x) = \begin{cases} 1 & \text{if } x \in \mathcal{A}, \mathcal{B} \\ 0 & \text{if } x \notin \mathcal{A}, \mathcal{B} \end{cases} \tag{2.6.1}$$

### 2.6.1 Rate calculation

With the new defined states $\mathcal{A}$ and $\mathcal{B}$ and their respective characteristic functions $h_{\mathcal{A}}$ and $h_{\mathcal{B}}$ the expression of the TIS rate constant looks similar to that of TPS, and it is defined as the derivative of a time correlation function related to the transition from $A$ to $B$,

$$k_{AB} = \frac{d}{dt} C(t)\Big|_{t=0}, \quad C(t) = \frac{\langle h_{\mathcal{A}}(x_0) h_{\mathcal{B}}(x_t)\rangle}{\langle h_{\mathcal{A}}\rangle}$$

$$k_{AB} = \frac{\langle h_{\mathcal{A}}(x_0)\dot{h}_{\mathcal{B}}(x_0)\rangle}{\langle h_{\mathcal{A}}\rangle} = \frac{\langle \Phi_{A,\lambda_B}\rangle}{\langle h_{\mathcal{A}}\rangle} \tag{2.6.2}$$

where $\langle \Phi_{A,\lambda_B}\rangle$ is the defined positive flux from $A$ through interface $\lambda_B$. The effective flux through an interface $\lambda_i$ is $\langle \Phi_{A,\lambda_i}\rangle$, and can be related to the effective flux of the interface before it, $\lambda_{i-1}$, by

$$\langle \Phi_{A,\lambda_i}(x_0)\rangle = \langle \bar{h}^f_{\lambda_i}(x_0)\rangle_{\Phi_{A,\lambda_{i-1}}} \cdot \langle \Phi_{A,\lambda_{i-1}}(x_0)\rangle \tag{2.6.3}$$

where $\langle ... \rangle_{\Phi_{A,\lambda_{i-1}}}$ is the ensemble average over all points in phase space for $x_0$ for which $\Phi_{A,\lambda_{i-1}}(x_0) \neq 0$ and the ensemble of the characteristic function is $\langle \bar{h}^f_{\lambda_i}(x_0)\rangle_{\Phi_{A,\lambda_{i-1}}} = \mathcal{P}(\lambda_i|\lambda_{i-1})$, the probability that a trajectory coming from $A$ will cross interface $\lambda_i$, given that it has passed interface $\lambda_{i-1}$ earlier in time. By applying this relation on all interfaces, the expression of the rate constant can be written as:

$$k_{AB} = \frac{\langle \phi_{A,\lambda_1}\rangle}{\langle h_{\mathcal{A}}\rangle} \prod_{i=1}^{n-1} \mathcal{P}(\lambda_{i+1}|\lambda_i) = \frac{\langle \phi_{A,\lambda_1}\rangle}{\langle h_{\mathcal{A}}\rangle} \mathcal{P}(\lambda_B|\lambda_1). \tag{2.6.4}$$

This expression allows for a calculation of the continous probabilities $\mathcal{P}(\lambda_{i+1}|\lambda_i)$ of crossing from state $A$ to $B$. The term for the effective positive flux have been reduced to the positive flux over the first interface $\langle\phi_{A,\lambda_1}\rangle$. Now (with a proper choice of order parameter and location of interfaces) this property can be calculated by a standard MD simulation by starting with a configuration of the system in $A$ and counting the number of effective crossings of $\lambda_1$.

The power of the interface sampling approach is that the crossing probability $\mathcal{P}(\lambda_B|\lambda_A)$, which for rare events can be extremely low, can be separated into probabilities $\mathcal{P}_A(\lambda_{i+1}|\lambda_i)$ that are much higher in probability.

### 2.6.2 The TIS algorithm

The complete procedure of the TIS scheme begins with a MD to calculate the flux $\langle\Phi_{A,\lambda_1}\rangle$ over the first interface, and as in TPS with the generation of an initial path of length $\mathcal{T}$ that starts out in $A$ and crosses the first interface $\lambda_i$ and then either ends back in $A$ or continues on to cross the next interface $\lambda_{i+1}$, see Figure 2.9. The initial phase space point $x_0$ is defined as the first point on the interface that crosses $\lambda_i$. Shooting moves are used at randomly chosen time slices but with a slight difference from TPS: instead of integrating forwards and backwards in time to a path of length $\mathcal{T}$, the integration is terminated once the path has reached the edge of either $\mathcal{A}$ or $\mathcal{B}$, see Equation (2.6.1), not spending time generating parts of the trajectory within either stable states.

Rejection occurs if the path does not reach the edge of $A$ backwards in time, or with a probability check: $\min\left[1, \frac{\mathcal{T}^{(o)}}{\mathcal{T}^{(n)}}\right]$, where $\mathcal{T}^{(o)}$ is the length of the old path and $\mathcal{T}^{(n)}$ is the length of the new one. An accepted path replaces the old one, the first crossing point of $\lambda_i$ is chosen as $x_0$ and the value of $\mathcal{P}(\lambda_{i+1}|\lambda_i)$ is measured. If the path length exceeds the max length of the new path, chosen by taking a random number $\alpha \in [0, 1]$ and calculating $\mathcal{T}^{(n)}_{\max} = \mathrm{int}(\mathcal{T}^{(o)}/\alpha)$, it is also rejected.

It is shown in Ref. 27 that by positioning the interfacces so that the general crossing probability of each interface is as close as possible to 0.2 one will obtain the highest efficiency of the rate calculations.

When using Monte Carlo moves in sampling techniques, any rejection of the trial path implies that the old path is counted again in the path ensemble and the

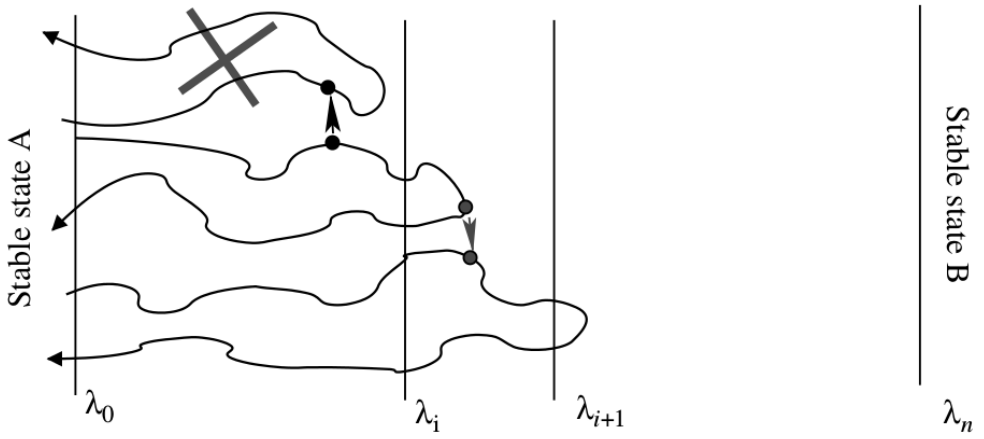


**Figure 2.9:** Illustration of the TIS path ensemble $[i^+]$ (positive crossing of $\lambda_i$), used to calculate the crossing probability of $\mathcal{P}(\lambda_{i+1}|\lambda_i)$. The shooting move is here applied to any point on the old path (middle) starting in $x_0$ and ending either in $\lambda_0$ or $\lambda_n$. The generated paths (top and bottom) are rejected/accepted respectively based on their crossing of interface $\lambda_i$. The top path is rejected, and the old path is recounted. The bottom path is accepted and even crosses the next interface $\lambda_{i+1}$, called a successful path. The fraction of successful paths against accepted paths determine $\mathcal{P}(\lambda_{i+1}|\lambda_i)$. Figure taken from article of van Erp [21].

process is restarted by choosing another shooting point [25].

### 2.6.3 Replica exchange and time reversal

In addition to shooting moves there is also a computationally cheap move called a *time reversal* move. The time reversal move takes a path or path segment in an ensemble, and reverses the direction of the path, switching the time slices from the beginning to the end and vice versa, reverting the velocities in the process as well [28]. This means that no force calcuations are required to generate the new path. If the old path is a non-reactive path, not visiting region $B$ the method will **always** generate an acceptable path, since the path being reversed had to be accepted in previous steps. Therefore two (or more) subsequent reversal moves should be avoided, as the second moves will have regenerated the original path used to generate the first new one.

The efficiency of both path and interface sampling can be greatly improved by

using the *path swapping* or *replica exchange* move [12, 29]. Similarly to shooting moves, path swapping is used to generate new trajectories from old ones, but by swapping accepted paths from neighbouring ensembles and checking if they cross the respective interface to the ensemble. This means that if a path in the ensemble for $\lambda_i$ also happen to cross $\lambda_{i+1}$ before returning to $A$, it can be succesfully swapped with the corresponding path in ensemble $\lambda_{i+1}$, as this path per definition crosses $\lambda_i$. The RETIS scheme substitutes the MD simulation of TIS with an additional $[0^-]$ ensemble, which contains paths that begin in $x_0$, but when integrated forwards in time moves *away* from interface $\lambda_0$ inside the region of $A$, before crossing the interface on its way *out* of $A$. This allows for a bit more flexibility of swapping moves by adding another ensemble to swap with. The $[0^+]$ ensemble behaves like other ensembles, leaving region $A$ to later return or reach region $B$. The $[0^-]$ ensemble is also used in the flux calculation of the RETIS scheme, which is defined in Ref. 12 as

$$f_A = \left( \left\langle \mathcal{T}_{\text{path}}^{[0^-]} \right\rangle + \left\langle \mathcal{T}_{\text{path}}^{[0^+]} \right\rangle \right)^{-1} \tag{2.6.5}$$

where the average length of path ensemble $[0^{+/-}]$ is $\langle \mathcal{T}_{\text{path}}^{[0^{+/-}]} \rangle$. The entire simulation is now defined by paths with interface-crossing properties that characterize them in different ensembles, and swapping between them becomes very efficient. In particular if the system studied has many possible reaction channels connecting $A$ and $B$ in phase space, introducing the swapping move will increase the efficiency of the calculation [29].

The swapping move is very cheap, and like the time reversal move it does not require any additional force calculations, except when swapping $[0^-]$ and $[0^+]$ (see Figure 2.10c). Like time reversal moves, subsequent swapping moves are also not favorable, as two swapping moves after each other, swapping between the same two interfaces, will have regenerated the original paths. However with a probability check on the $[0^-] \leftrightarrow [0^+]$ swap, two subsequent swapping moves could avoid regenerating old paths in ensembles by first swapping $[0^-] \leftrightarrow [0^+]$ and then in the next step swap $[0^+] \leftrightarrow [1^+]$, or vice versa.

The swapping move is implemented with the TIS algorithm so that there is a probability check each cycle to do either shooting, time-reversal or swapping

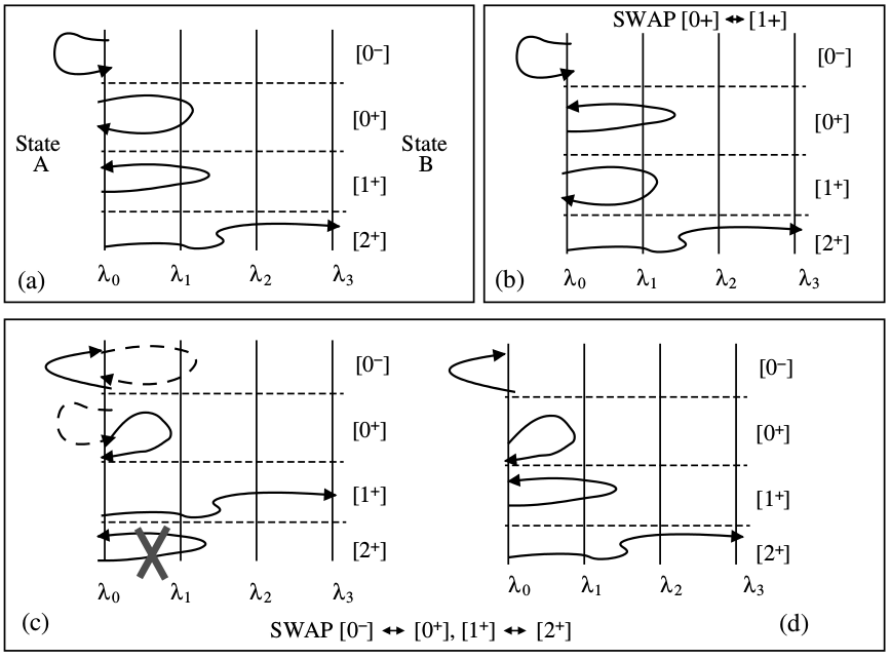


**Figure 2.10:** Illustration of the swapping move in RETIS scheme with four interfaces $[0^-]$,$[0^+]$,$[1^+]$ and $[2^+]$. (a) shows the old state, with one path in each of the four ensembles. (b) illustrates the swapping of paths in ensemble $[0^+]$ and $[1^+]$, which is accepted because the original path in $[0^+]$ is valid in $[1^+]$ since it also crosses $\lambda_i$. (c) shows the attempted swap of $[0^-] \leftrightarrow [0^+]$ and $[1^+] \leftrightarrow [2^+]$. The dashed lines show the two new path generated in $[0^-]$ and $[0^+]$, which are valid in the their respective ensembles. However, since the path in $[1^+]$ is not valid in $[2^+]$ the swap is rejected and the original paths are recounted to give the resulting state in (d). Figure taken from article of van Erp [21].

moves. In the case of shooting moves, all the path ensembles will be updated by attempting to do one shooting move. In the case of a swapping move, and if the move is accepted, the two segments are either just swapped or in the case of $[0^-] \leftrightarrow [0^+]$, integrated forwards and backwards in time as shown in Figure 2.10(c). When swapping the $[0^-]$ and $[0^+]$ ensembles, the last time step in $[0^-]$ is used as the initial point and integrated forwards in time to generate a new trajectory in the $[0^+]$ ensemble, and the initial point in the old path $[0^+]$ is integrated backwards in time to generate a $[0^-]$ path [12]. And again, if the paths swapped do not cross the relevant interfaces to the ensemble, they are rejected.

# Chapter 3

# Implementation

In this chapter we will describe the implementation of the Stillinger-David potential and the QChem interface with the TIS dynamics program. We will also define the orderparameter used for the reaction, illustrating the system, initial conditions and define states $A$ and $B$ of the reaction.

## 3.1 Implementing the code

The simulation were preformed using the dynamics program TISMOL, written in Fortran 90 by Titus van Erp et al. The program code gives the rate constant and transmission coefficient of the reaction, with error calculations for crossing probabilities and forward flux, as well as statistics on shooting moves, path lengths, etc.

The Stillinger-David pair-potential functions of Stillinger and David [5] were written to fit the code of van Erp's, including the derivatives for the coulombic forces. The parameters for the three pair potentials, two screening functions, particle charge and dipole polarizability were chosen set as in the original article. The polarization potential and corresponding forces were taken from the source code used by Geissler, Dellago and Chandler [9], which Christopher Dellago was so kind to send to us.

In order to do calculations using the Coupled-cluster approximation we needed to use an external program to do the electronic calculations. We chose to use

the electronic structure program QChem, described in publications by Kong et al. [30], Shao et al. [31, 32], and on the official webpage [33]. An interface with the quantum chemical program CFour [34] was also created, but not used due to errors with the code on the cluster.

For the coupled-cluster calculations in QChem, an interface with van Erp's code was written, so that the relevant energies and energy gradients were extracted and read by the dynamics in the RETIS scheme, then an input file with coordinates was written to be executed by the QChem code on the NOTUR cluster Stallo[35].

## 3.2 System and order parameter

The order parameter chosen for this simulation was the one used by Geissler et al. [9] on the same protonated water trimer system. The orderparameter is defined as the difference between two angles between oxygen atoms in the system, calculating the difference between the initial hydronium ion and the two neighouring oxygens, and between one of the neighouring oxygens and its respective oxygen neighours, see Figure 3.1.

$$\Delta\theta = \theta_2 - \theta_1 \tag{3.2.1}$$

This orderparameter gives a value $\Delta\theta \approx -1.6$ in initial state $A$ and similarly $\Delta\theta \approx 1.6$ in end state $B$, as shown in Figure 3.2, and therefore the range in the orderparameter over the reaction is {-1.6,1.6}, but we use $\lambda_{\mathcal{A}} = -1.50$, to allow the system some freedom of movement in the $[0^-]$ ensemble, and $\lambda_{\mathcal{B}} = 1.50$ to have the initial and end state mirror each other.

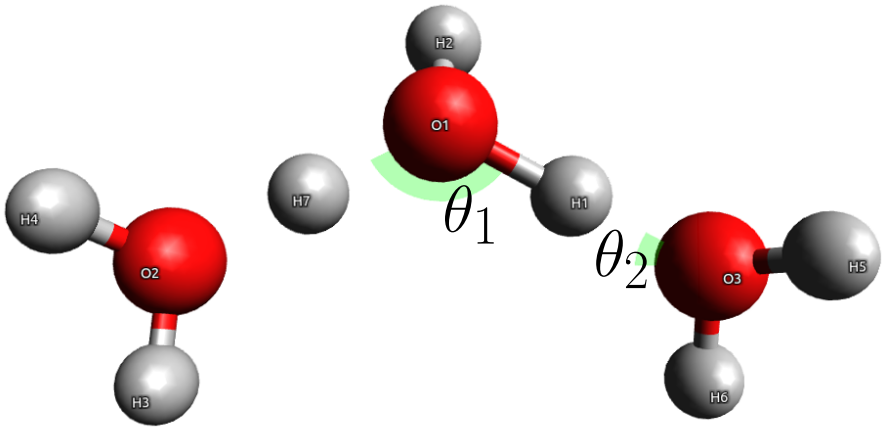


**Figure 3.1:** The orderparameter $\Delta\theta = \theta_2 - \theta_1$ chosen for the protonated water trimer, oxygen #1 and the surrounding three hydrogens compose the initial hydronium ion. The order parameter should promote the system to follow a certain trajectory so that oxygen #2 will be the new center of the trimer, see Figure 3.2.

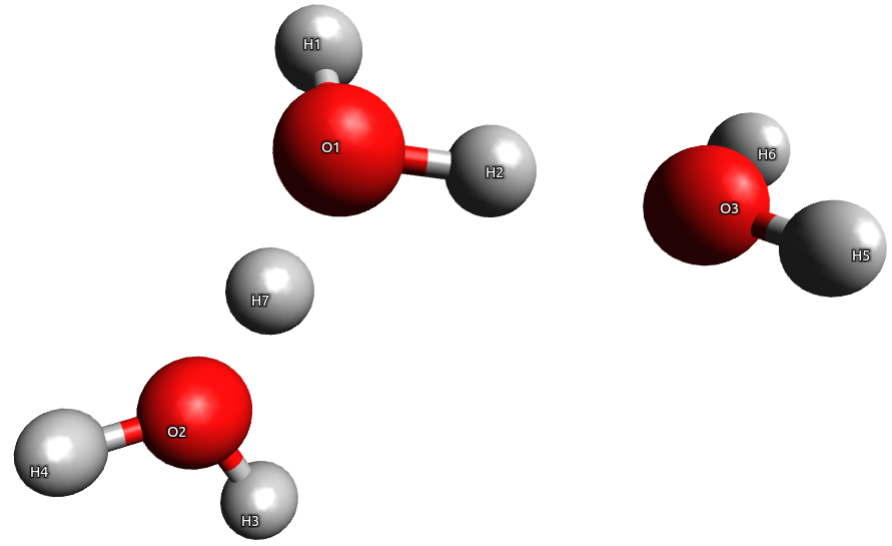


(a)

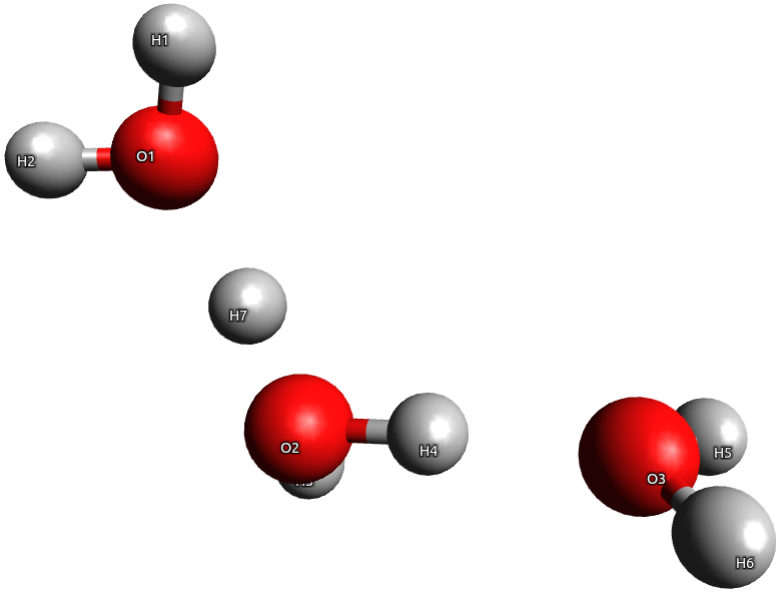


(b)

**Figure 3.2:** Illustration of the water trimer system. The initial state (a) and the end state (b) of a complete path from the simulation using the Stillinger-David potential. The excess proton, labeled H7, starts out bonded to O1 in (a), but after the transition to (b) will have transfered to O2

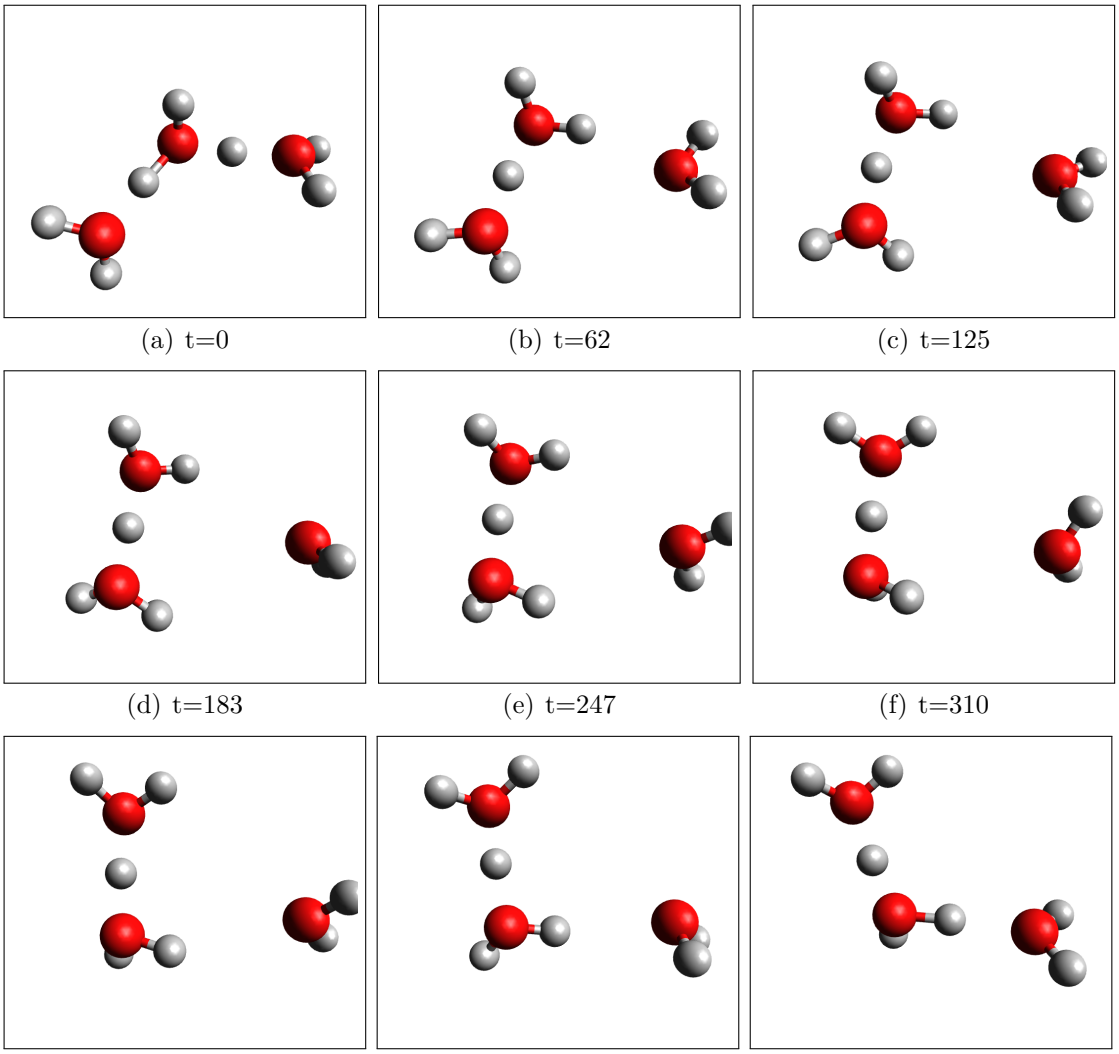

(a) t=0 (b) t=62 (c) t=125

(d) t=183 (e) t=247 (f) t=310

(g) t=373 (h) t=433 (i) t=492

**Figure 3.3:** Illustration of a reactive pathway generated during the TIS simulation in section 4.2.1. The lenght of the path between states $A$ (a), and $B$ (i), was $\sim 500$ time steps long, or approximately 250 fs. (d) shows the system at the proposed transition state, with the excess proton located more or less equidistant from the two closest oxygens. The length of this reactive pathway agrees well with the trajectory illustrated in Ref. [9]

## 3.3 Details for the Stillinger-David simulations

For the TIS simulation using Stillinger-David potential we tried to use the same parameters for the system as done by Geissler et al. [9] – to compare our result for the rate of reaction with theirs. When using the energy units [kcal/mole], length [Å], etc., the unit of time $\tau$ is calculated to be 48.887 fs. To get a small enough $dt$, we chose to use $dt = \tau \times 0.01 = 0.48887$ fs, at a temperature of 300 Kelvin, and with interfaces between states $A$ and $B$ positioned as shown in table B.1 in Appendix B. The reason for not having any other interfaces than $\lambda_B$ with positive values, is that once the last interface at $\lambda(x) = -0.10$ is crossed, the trimer will likely still have enough kinetic energy to continue past the transition state at $\lambda(x) = 0.00$ and down into the potential energy well of state $B$ with certain probability.

A TIS simulation was first run for a total of 1000 cycles, giving a couple of good paths to use as seed for the actual simulation. Every trajectory but the last accepted one in each ensemble was discarded, and the simulation was restarted, using these trajectories as the initial path of the new ensembles. This was done to avoid including the initial paths created by the system in the rate calculation. The simulation was restarted, for a total of 400000 cycles, and the rate constant was calculated.

The same approach was done when running the RETIS simulation of the same system; 1000 cycles with only shooting moves to get good paths as seed for the simulation. The interfaces, and the random distribution of shooting, swapping and time reversal moves are shown in table B.2 in Appendix B. The full RETIS siimulation was also run for 400000 cycles, also giving a rate constant. The choice of 25% for the swapping move and time reversal moves was made as to avoid having situations where either two time reversal moves on the same ensemble happen subsequently, or several swapping moves in sequence.

## 3.4 Details for the Coupled-cluster QChem simulation

For the coupled-custer theory we used the 6-31g(d) Gaussian-type orbitals as basis set for the total wavefunction, because the system is very simple, without any larger molecules than hydronium ions and not many particles in total. We used CCSD (single and double excitations) level of theory for the energy calculation, and a tolerance for convergence of all energy calculations of $10^{-7}$.

To get the forces for the dynamics, Qchem was called to do a geometry optimization of an input file written with the current configurations of the system. But the optimization was terminated after 1 cycle, so that the full analytical gradient could be obtained from the Qchem output file, without having changed the configuration of the system. The unit of time $\tau$ for these simulations was calculated to be 1.032728 fs, and we therefore used a time step $dt = \tau \times 0.5 = 0.516364$ fs for the simulations.

For the MD simulations we tried two different simulations of 1000 steps, both starting at a phase point close to the proposed transition state. The hope was to generate a forward and backward path from this point, to see if the CC simulations gave results comparable to the SD simulations.

# Chapter 4

# Results and Discussion

In this chapter we present the results from the different simulation we performed. We will first look at the relative bonding of excess protons in the water trimer, using the proposed Transition state and order parameter to promote the catalyzed proton transport. Then we present the TIS/RETIS results, discussing the difference between our simulations and that of Geissler et al. [9].

Lastly, we discuss the success of our QChem interfacing, using quantum chemistry methods in path sampling and future work.

## 4.1 Relation between O-H distance and $\Delta\theta$

To illustrate how the bonding behaviour of the excess proton (labeled H7 in Figures 3.1 and 3.2) in the trimer changes with the Oxygen-Oxygen angle order parameter, we plotted the relation between the orderparameter and the distance between the excess hydrogen in one of the (possibly several) complete paths harvested in the SD-TIS simulation, which connected the states A and B, in Figure 4.1.

From the plot in Figure 4.1 we can see how the excess proton behaves throughout a reaction pathway connecting A and B. The order parameter does not discretize the stable states on the distance between Oxygen and hydrogen, but in this plot we can see a correlation between the two transitions. Initially in state A the hydrogen, labeled H7 in Figure 3.1, is considered to be bonded with the Oxygen atom labeled O1, with an average bond distance of about 1.1–1.2 Å. When the

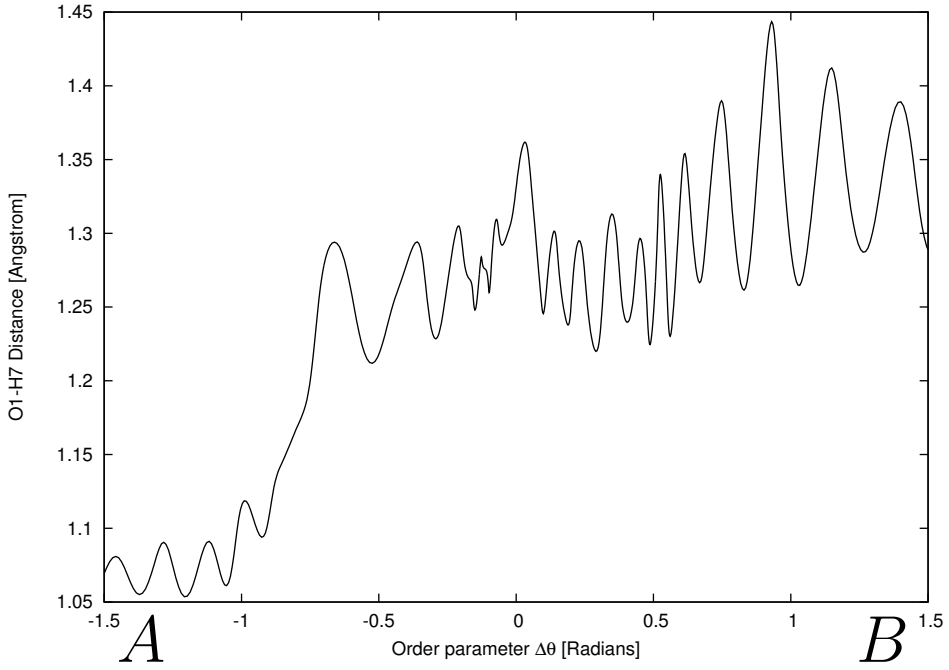


**Figure 4.1:** The bond distance of O1 and H7 (see Figure 3.1) during one of the reactive pathways (Figure 3.3) generated by a TIS simulation at 300K in section 4.2.1. Distance plotted over order parameter; states A and B marked on the x-axis, and Oxygen closest to H7 marked on the y-axis. Just before crossing the TS at $\lambda(x) = 0$, the O1-H7 bond is broken, and after crossing the H7-O2 bond is formed.

system approaches the transition point $\lambda(x_t) = 0$ we can see that the hydrogen starts to drift away from the first Oxygen atom and approaches the second Oxygen atom. After succesfully crossing over and towards state $B$ we see that the hydrogen atom moves further away from the first Oxygen, ending at a distance of about 1.45 Å when the system crosses into the defined region B. The distance traveled is not that large: in simple MD simulations this result could be achieved without much effort, as shown in Figure 4.2.

From the distribution in Figure 4.3 (and somewhat from the plot in Figure 4.2) we can see that most of the time, all three hydrogens in the hydronium ion stay within a radius of 1.3 Å from the Oxygen, except for a few steps where one of the protons briefly jumps to a neighouring Oxygen, with a distance up to 1.7 Å.

This jumping between two Oxygens is common, as the figures show, it occurs

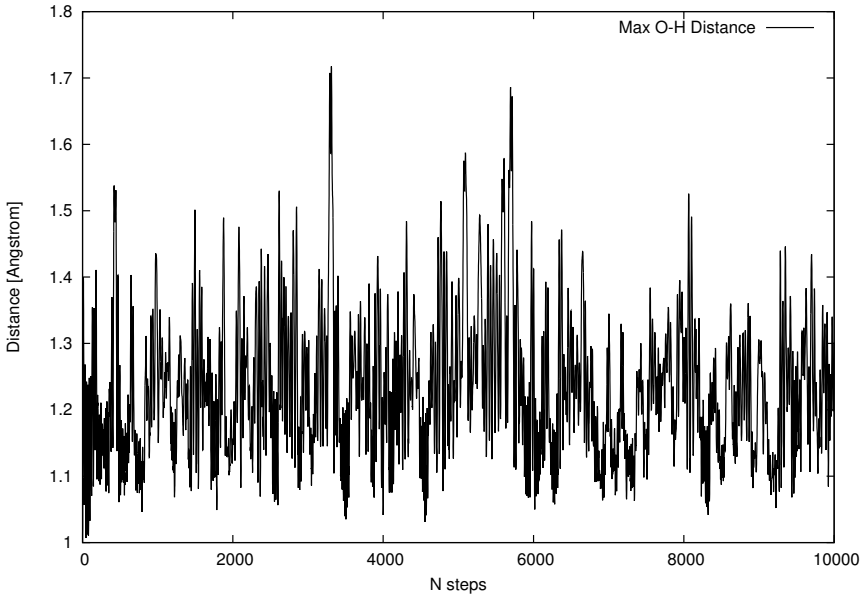


**Figure 4.2:** Maximum O-H bond distance of the three possible bonds in the hydronium ion plotted over time from a NVE MD of $N = 10000$ steps, using the SD potential.

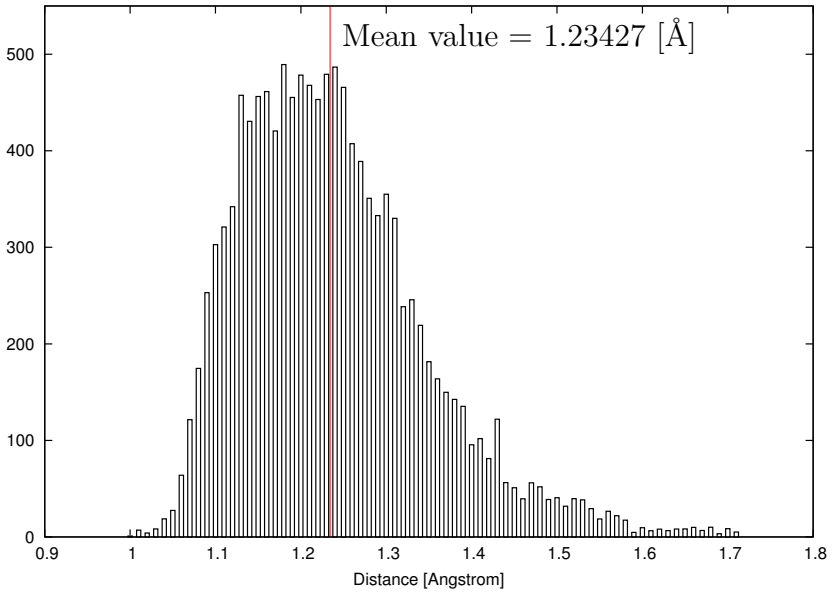


**Figure 4.3:** Distribution of the maximum O-H bond distance from the MD simulation illustrated in Figure 4.2. Average of the maximum bond distance 1.23427Å indicated by the red line.

two or three times within about 4–5 ps. Neighbouring hydrogens in the hydronium ion repel each other with a sufficient force to make this back and forth transition happen quite rapidly. The proton will, however, spend relatively more time bonded to the center oxygen then to either of the neighbour oxygens, due to the overall attractive forces from the oxygen charge and polarizable dipole which neutralize the repulsive forces from the other two hydrogens.

It is important to remark, however, that this catalyzed transport reaction differs from the simple "jumping back-and-forth" in between neighbouring Oxygens that the proton will display in such a simulation. By looking at where the excess proton spends *most* of the time during the simulation we can decide whether and where it is, or isn't, bonded to an Oxygen. The proposed TS and reaction pathway of Geissler et al. [9] solves this by instead of looking specifically at the protons of the system, which as explained will transfer on their own, we look at how the oxygens are positioned in relation to one another. That is why this specific reaction shows how the excess proton can be succesfully transferred to a neighbouring Oxygen, which has become the new center of the trimer system. This particular transfer of protons is very limited to this exact system, since the transition relies on there being a "center" Oxygen to the whole system, which the excess proton will bond to in order to equally disperse the proton charges.

### 4.1.1 Potential energy barrier along the reaction pathway

We also plotted the potential energy calculated at each time slice in Figure 4.4, following the system through the reaction path connecting state A and B, to see how the potential/free energy of the system changed during the path in reaction Figure 3.3 and 4.1.

In Figure 4.4 we can see the characteristic energy curve dividing the stable states A and B, almost as imagined in TST, over the order parameter. With stable states A and B at a potential energy of approximately $-3322$ [kcal/mole], and the transition state at $\Delta\theta = 0$ at around $-3308$ [kcal/mole], giving the activation energy of this reaction pathway to be 14 kcal/mole. The energy curve is noisy, due to the vibration of O-H bonds in the trajectory. Therefore, an exact activation energy cannot be determined from a single path. An additional illustration was

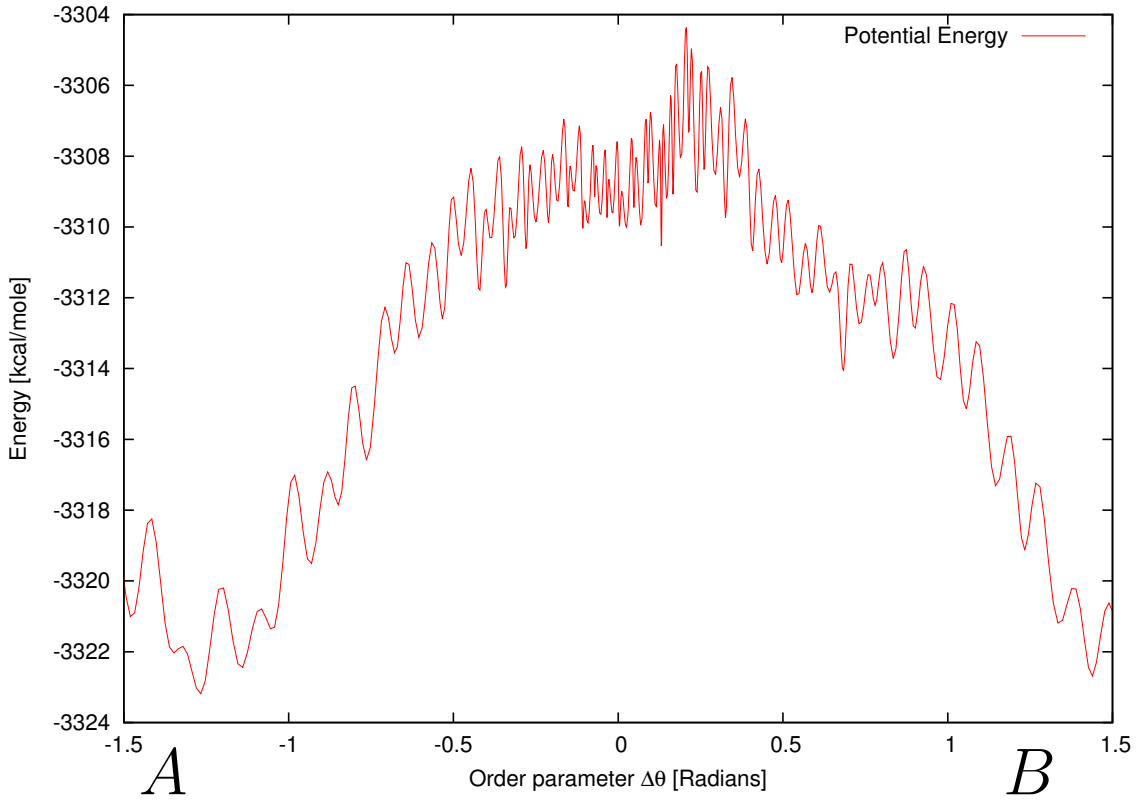


**Figure 4.4:** The potential energy of the system through the reactive pathway which was illustrated in Figure 3.3. The potential energy behaves much like proposed in TST, with a high barrier the system has to cross in order to complete the reaction. The noise is a result of the rotations and vibrations of the O-H bonds during the transition.

generated, by averaging the paths and trajectories in the 14th ensemble of the TIS simulation, to create a surface plot illustrating the stable states $A$ and $B$. Figure 4.5 shows the potential energy surface. Since the surface is generated from only one ensemble, the exact energy of the states are not correct, due to defining states by $\Delta\theta = 1.5$ and $-1.5$. The figure does, however, illustrate nicely the potential surface of the system and reaction, and the relevant O-H distance in state $A$ and $B$.

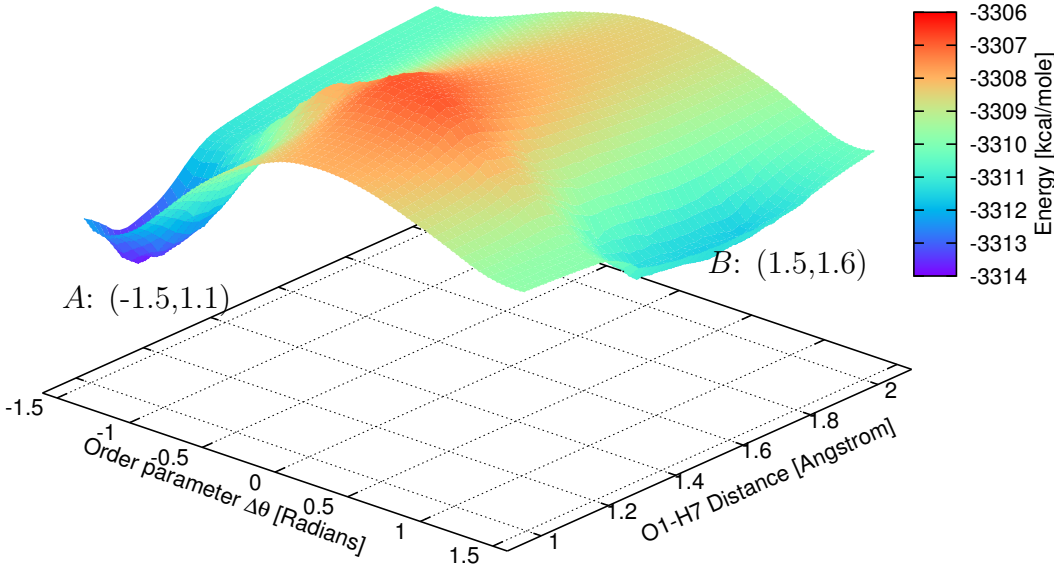


**Figure 4.5:** The potential energy surface, generated from averaging all complete paths and trajectories in the $\lambda_{14}$-ensemble of the TIS simulation. Potential energy (z-axis, color scheme) depending on the order parameter $\Delta\theta$ of the system (x-axis), and the distance $r(O_1, H_7)$ (y-axis). Stable states $A$ and $B$ as indicated on the figure {x,y}, in potential energy wells at (-1.5,1.1) and (1.5,1.6), respectively.

## 4.2 Stillinger-David simulations

With the Stillinger-David potential we did two simulations, using regular TIS with shooting moves and RETIS with swapping moves and time reversal moves, respectively. The setup used both for the TIS and RETIS scheme initially gave us transition paths and interface crossing paths that differed greatly from both the referance paper [9] and what should physically be possible for our system. For instance, the trajectory that connected state A and state B was successful in moving the proton, by moving the centre oxygen (O1) to the side and getting a new centre of the trimer. But during the transition the distances between the traveling

water molecule and the other two, the oxygen-oxygen distances in the trimer were up to, and sometimes above, 7 Å. An illustration of just one of these randomly generated initial paths is shown in Figure 4.6, where we have a non-reactive path: a path starting in state A, crossing the 14th interface at $\Delta\theta = -0.10$ and returning back to state A, with one of the water molecules shifted $\approx 4$ Å from the centre. These trajectories did not represent the transition as proposed by Geissler et al. [9], since they allowed too much space in between the water molecules in the system. After about 1000 TIS cycles, however, this distance was shortened down, so that the transition had an O-O distance within $\sim 4$ Å. This happened because the initial paths with a large O-O distance was higher in energy than the paths with shorter distance, and for every iteration with a shooting move there would be a path created with a shorter O-O distance. The shorter paths were lower in energy than the longer ones, because the long paths essentially removed an entire water molecule partially away from the system before returning it; to achieve this a lot of energy is required. By deleting the first 1000 cycles the simulation, we ensured getting rid of the unphysical initialization effects, and we got paths more akin to the one illustrated in Figure 3.3.

It is worth noting that this kind of problem would have a much lower chance of occuring if we had chosen to define our stable states with order parameter values closer to the TS, as the system would have a smaller range of the order parameter to change the configuration as much as observed above. However, the unrealistic paths were quickly discovered and removed from the ensemble, not interfering with our results.

### 4.2.1 TIS simulation without swapping and time reversal

We first did a standard TIS simulation of the water trimer system using the Stillinger-David potential, using only the shooting move to harvest paths for the path ensemble. After removing the first 1000 cycles of the simulations, we restarted and ran for a total of 400000 cycles. With the interfaces in between the defined states of $\mathcal{A}$ and $\mathcal{B}$ as described, we obtained the flux $f_{\mathcal{A}}$ using eq. (2.6.5) and the total crossing probability, $\prod_{i=0}^{14} P(\lambda_{i+1}|\lambda_i)$, calculated from the product of individual probabilities in table C.1. Distribution of crossing probabilities is shown in

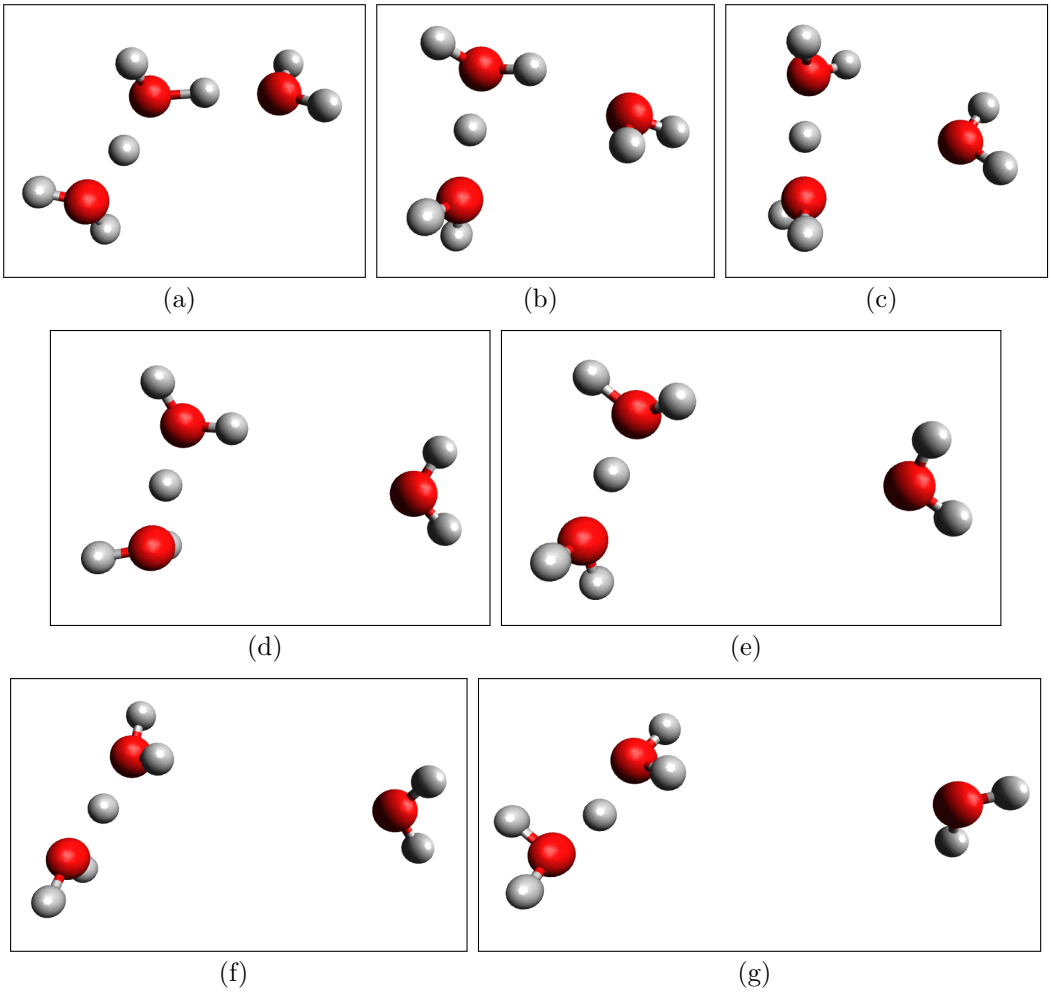


**Figure 4.6:** Time slices (a–g) of a pathway generated in initialization, initial configuration for state A in (a) and end configuration in (g). The trajectory of the system crosses the next to last interface ($\Delta\theta = -0.10$) in (c) before state B, and then returns back to state A. In (a) the system is close to the equilibrium configuration, with an O-O distance of $\approx 2.5$Å, but at the end of the path in (g) the distance measured between the centre and rigthmost oxygen is $\approx 6.35$Å.

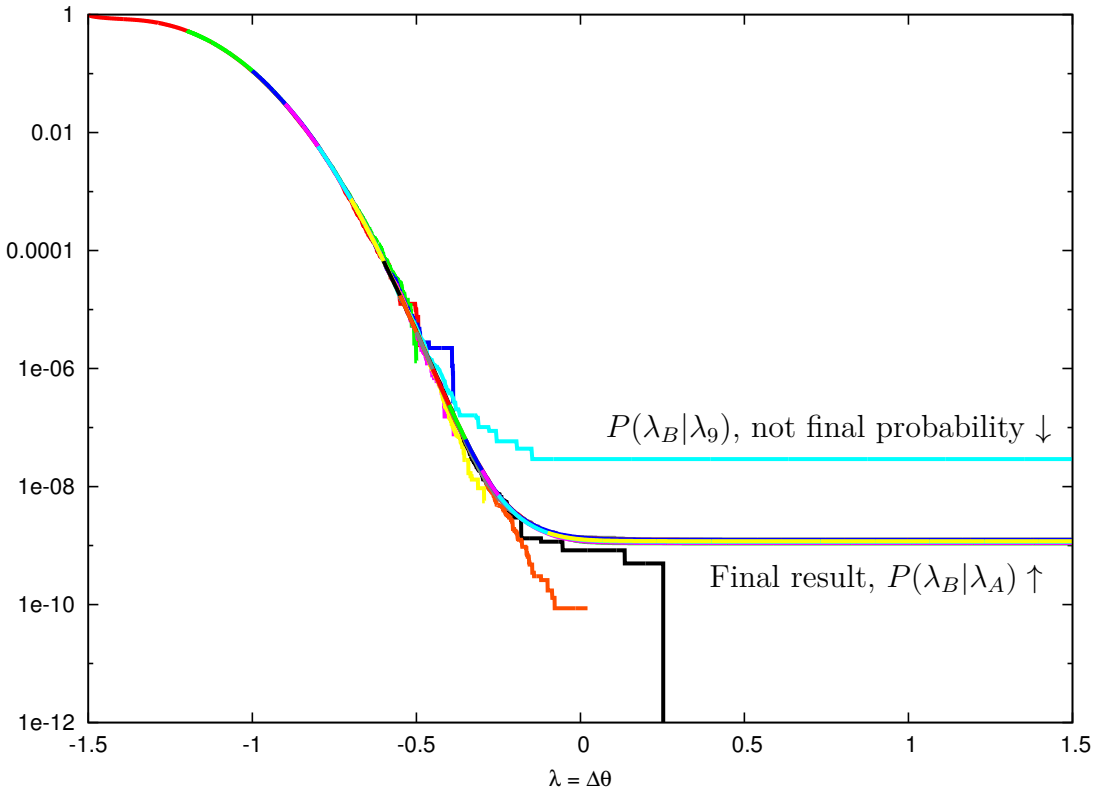


**Figure 4.7:** The total crossing probability of the Stillinger-David TIS simulation. Distributions of the measured order parameter in each ensemble throughout the simulation have been rescaled using the corresponding crossing probabilties, to give a plot of the overall probability distribuition. Final crossing probability $P(\lambda_B|\lambda_A)$ located as indicated in the figure, where distribution of ensemble 14 crosses $\lambda = 1.5$, but is hard to spot since ensembles 10-14 are grouped so close together. Ensemble 9 is the light-blue, outlying plot also indicated, but its end-value is not the final result for $P(\lambda_B|\lambda_A)$, but the scaled up crossing probability of $P(\lambda_B)|\lambda_9)$.

Figure 4.7, and flux, product of crossing probabilities and rate of reaction shown in table 4.1.

The rate of reaction is initially calculated as a rate per time step for the simulation. The rate of reaction, using the TIS scheme with only shooting moves and a unit of time of 48.887 fs, is calculated to be $3.8168 \cdot 10^3 s^{-1}$.

In Figure 4.7 we can see that crossings into state B actually occurs in ensembles other than $\lambda_{14}$, with very low relative probability of crossing. Ensembles 10–14 all contain paths that cross into the region of state B, but with such low occurence in

| | Symbol | Value | [unit] | Error(%) |
|---|---|---|---|---|
| Flux out of region $A$ | $f_{\mathcal{A}}$ | 0.15762 | $\tau^{-1}$ | 0.32593 |
| Crossing probability | $P(\lambda_{\mathcal{B}}\|\lambda_{\mathcal{A}})$ | $1.18382 \cdot 10^{-9}$ | | 5.44404 |
| Rate of reaction | $k_{AB}$ | $1.86594 \cdot 10^{-10}$ | $\tau^{-1}$ | 5.45379 |
| | | $3.81680 \cdot 10^{3}$ | $s^{-1}$ | |

**Table 4.1:** Table of results from the TIS simulation using the Stillinger-David potential. The flux $f_{\mathcal{A}}$ over interface 0, total crossing probability $P$ (from table C.1) of paths crossing from $\lambda_A$ to $\lambda_B$, $t^{-1}$ is per time unit ($t = 48.887$ fs), and $k$ the rate of the reaction. All values with the relative (%) error calculated using block averaging.

ensembles 10 to 13 that they are all grouped together in the figure, even after being scaled to fit. The outlying line in the figure is of ensemble 9, $\lambda_9 = -0.45$, which present what appears to be a relatively higher crossing probability to state $B$ than the ensembles following it. While this may look like an apparent error in the choice of interfaces, that the crossing into state B could be achieved from a state with the value of the order parameter 0.45 radians away from the proposed transition state, the actual probability of this crossing is miniscule. When illustrating only the distribution of ensemble 9 in Figure 4.8 this becomes clear. From the distribution in Figure 4.8 we can see that the occurence of paths connecting state A and B in the $\lambda_9$ ensemble is extremely low, $\sim 0.3\%$. With 400000 cycles, there are still a substantial number of reactive paths in this ensemble, which when scaled up relative to subsequent ensembles in Figure 4.7 appear to be significant. This is not the case however, and in order to get the most efficient and accurate calculation of the rate, we need to use all ensembles we have defined.

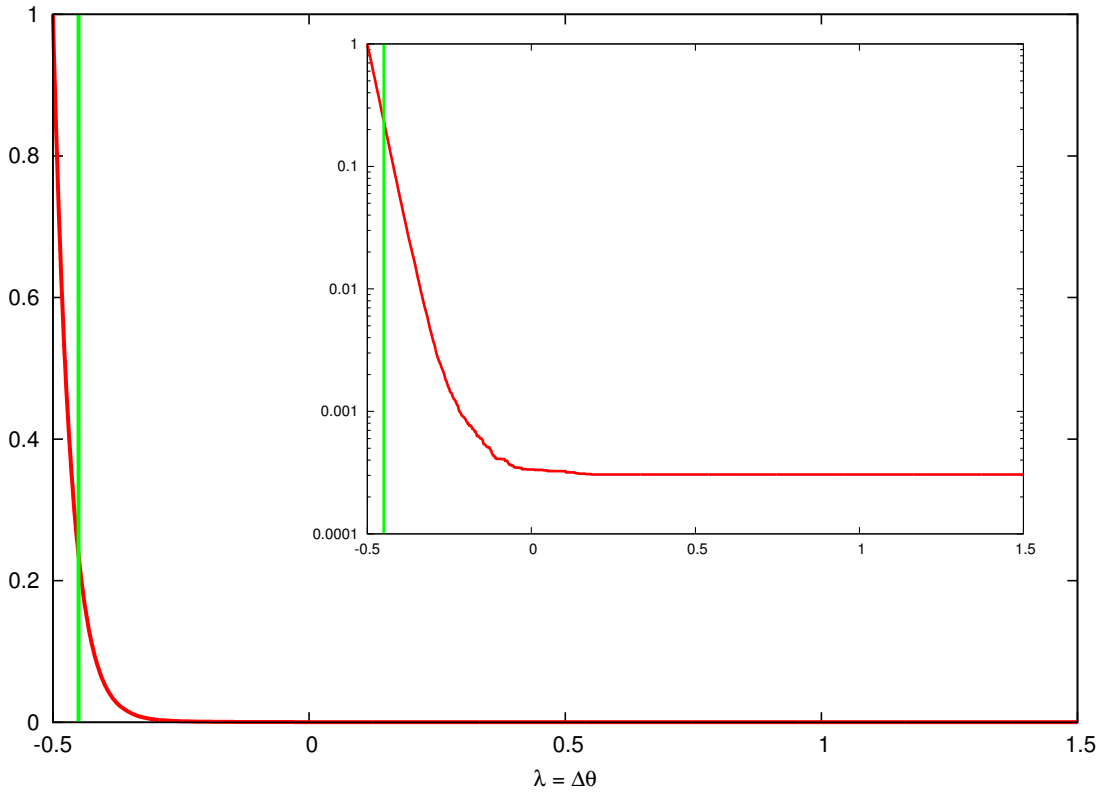


**Figure 4.8:** Illustration of the probability distribution of paths (red) of the $\lambda_9$ ensemble and with the interface line (green). The intersection of the interface line and the crossing probability gives us $P(\lambda_9|\lambda_8)$, see table C.1. At the end of the plot the value for the relative distribution of the path is $3.05 \cdot 10^{-4}$. Inset shows the same distribution with a logarithmic scale.

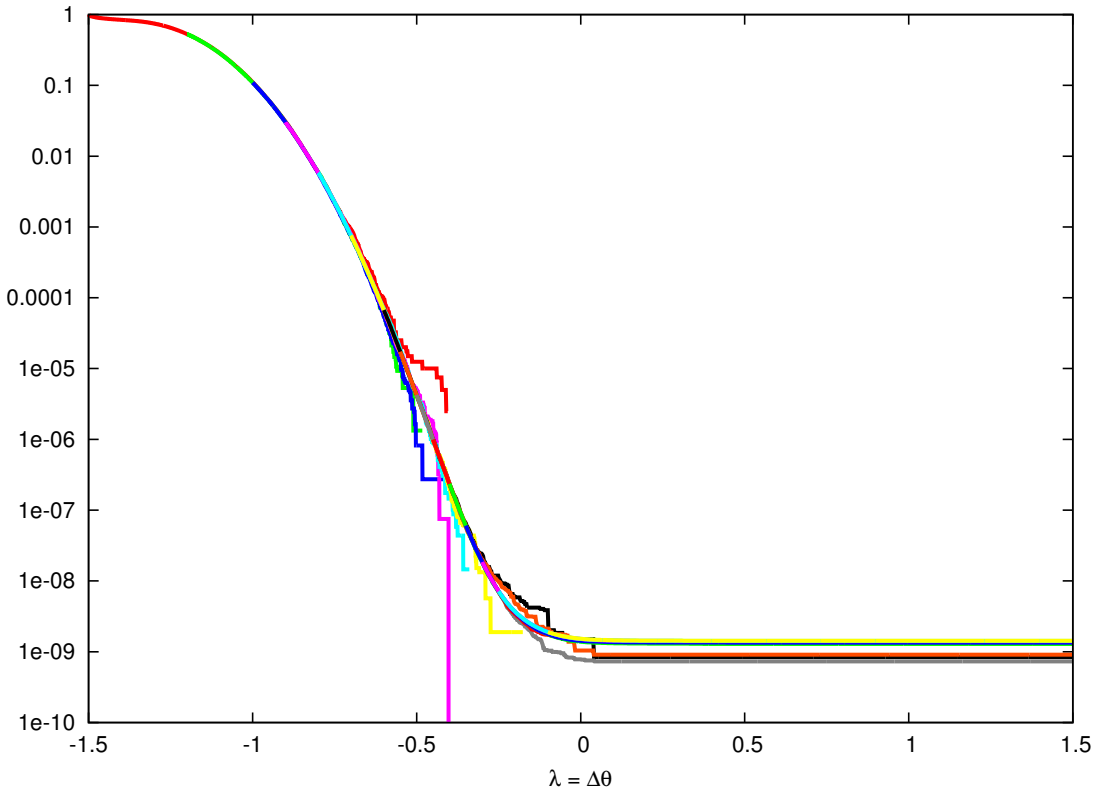


**Figure 4.9:** The total crossing probability of the Stillinger-David RETIS simulation. Distributions of the measured order parameter in each ensemble throughout the simulation have been rescaled using the corresponding crossing probabilties, to give a plot of the overall probability distribuition.

### 4.2.2 RETIS simulation with swapping and time reversal

Just like the TIS simulation, the RETIS simulation was restarted and run for a total of 400000 cycles, after removing the first 1000 cycles. The interfaces were defined like for the TIS simulation, which is shown in table B.2, with the frequencies for the three path sampling moves.

Using the flux $f_A$ per unit of time, crossing probability $P(\lambda_B|\lambda_A)$ as above, we found the rate of reaction with the RETIS scheme to be $4.61742 \cdot 10^3 s^{-1}$, slightly different from the one obatined using TIS. The main difference between the two techniques is that we achieved a higher total crossing probability from all interfaces when using RETIS. Still, given the very small overall probability the relative agreement of the two methods should be considered as very good. As both

| | Symbol | Value | [unit] | Error(%) |
|---|---|---|---|---|
| Flux out of region $A$ | $f_{\mathcal{A}}$ | 0.15787 | $\tau^{-1}$ | 0.25309 |
| Crossing probability | $P(\lambda_{\mathcal{B}}\|\lambda_{\mathcal{A}})$ | $1.42986 \cdot 10^{-9}$ | | 6.80686 |
| Rate of reaction | $k_{AB}$ | $2.25732 \cdot 10^{-10}$ | $\tau^{-1}$ | 6.81156 |
| | | $4.61742 \cdot 10^{3}$ | $s^{-1}$ | |

**Table 4.2:** Table of results from the RETIS simulation using the Stillinger-David potential. The flux $f_{\mathcal{A}}$ over interface 0, total crossing probability $P$ (from table C.1) of paths crossing from $\lambda_A$ to $\lambda_B$, $t^{-1}$ is per time unit ($t$ = 48.887 fs), and $k$ the rate of the reaction. All values with the relative (%) error calculated using block averaging.

simulations calculates the flux over the same interface with the same conditions, the flux from both techniques is almost identical, and when considering the relative error they overlap and can easily be assumed equal.

Additionally, we do not observe an outlying ensemble with a relatively larger occurence of reactive paths as in the TIS scheme. The reason for this could be that a randomly generated path in the $\lambda_9$ ensemble, as was observed in TIS, would be swapped quite frequently with neighbouring ensembles. Thus none of the ensembles would appear as $\lambda_9$ does in Figure 4.8. This results in a faster convergence of the simulation, which was proved in Ref. 12.

### 4.2.3 Comparing sampling techniques and results

When comparing our results with that of Geissler et al. [10], it is clear that our results for the rate of the reaction differ greatly from theirs, with both our calculated rate of $3.81680 \cdot 10^3 s^{-1}$ from the TIS simulation and $4.61742 \cdot 10^3 s^{-1}$ from the RETIS simulation being much lower than those reported from DFT. Geissler et al. reported a rate of $k = 2.3 \times 10^8 s^{-1}$ for a low energy transition, and $k = 1.1 \times 10^8 s^{-1}$ for a high energy transition. In the TIS/RETIS approach we did no separate analysis on these low and high energy transition states, as described in Ref. 9. This could be done with post-analysis on the stored ensembles, but would not correct

the large difference between our calculated rate and that of Geissler et al.

Concerning the rate of reaction, Ref. 9 shows the results of a log(k) versus energy plot, but does not provide the normalization factor to which k has been divided to make it dimensionless. On the other hand, Ref. 9 provides a graph of the correlation function, $C(t)$, for a fixed conserved energy which should be comparable with our room temperature calculations. From the slope of the graph we deduct that the rate constant is $2.5 \times 10^{-5} s^{-1}$ which is about 13 orders of magnitude lower than the DFT result. This seems too much. Possibly the time unit along the x-axis or the large scaling ($10^{16}$) factor given in the graph was an error. We asked the authors about this but since this was shortly before the submission deadline of this thesis we can not report their answer here.

From Equation 2.6.4 we have that the reaction rate is relying on mainly two terms: the flux out of state $A$ ($\Phi_{A,\lambda_1}$ or $f_A$), and the total crossing probability from the first interface and all the way into state B. By extending the range of the order parameter, we lower the general probability that any path created will connect states $A$ and $B$. Also since the potential energy of the system is at a maximum at the TS, $\Delta\theta = 0$, and two energy wells at $\Delta\theta < -1.5$ and $\Delta\theta > 1.5$, crossing probabilities of trajectories in between stable states and transition state will be considerably less than 1, confirmed by the results in tables C.1 and C.2. This will again result in a very low total crossing probability $P(\lambda_{\mathcal{B}}|\lambda_1)$, which gives a low rate. In principle the rate calculation should result in the same rate, also when positioning $\lambda_0$ at $\Delta\theta = -0.10$, since the flux should be significantly lower for this interface.

An attempt was made to do the TIS simulation with the states $A$ and $B$ defined by $\Delta\theta < -0.10$ and $\Delta\theta > 0.10$, respectively. Unfortunately there was an issue in the intialization of a path for the $[0^-]$ ensemble. Since the $[0^-]$ path has to be moving *away* from the transition state, and with the interface being located close to the top of the energy barrier, this resulted in that the system got trapped in the potential energy well in and around state $A$. We were unable to get the system back up the energy barrier after this, even when increasing the maximum path length to 50000, which made the laptop running the simulations at the time crash due to a lack of memory to allocate for the path. By assuming that both the simulations from -1.5 to 1.5 and from -0.1 to 0.1 would by principle result in the

same rate, the flux over the first interface of this short transition would have to be in the order of $10^{-10}dt^{-1}$. This would again mean, according to Equation (2.6.5), that the sum of average path lengths in $[0^-]$ and $[0^+]$ would have to be in the order of $10^{10}$, a much larger maximum pathlength than what crashed our simulations.

#### Deviations between SD potential and source code

We should also mention that we discovered a difference between the source code of Geissler et al. provided by Christopher Dellago. When comparing equation 2.2.8, the Coulombic repulsion between oxygens in the code, with the same equation in the original article [5], there was a difference in the final term. This results in a very small deviance in the potential energy at close distances, lower than $\sim 2.45$. This deviance is shown in Figure 4.10.

$$\phi_{OO}(r) = \ldots + e^{-6(r-2.70)} \qquad \text{Potential of Stillinger and David}$$
$$\phi_{OO}(r) = \ldots + e^{-6(r-2.70)^2} \qquad \text{Potential of Geissler et al.}$$

It is however very unlikely that this error would have any influence on the results. The deviance is simply too small, and at such short O-O distances, that the system would never reach a point where this difference becomes relevant. The energy required to force two oxygen atoms that close together is enormous.

## 4.3 Coupled-cluster simulation

We first needed to test the interface created, proving the consept by doing a standard MD simulation with energy and force calculations from the CC program. Then we tried to run a MD calculation starting out in a configuration close to the TS for the system, to generate half a reactive path using CC. Lastly we tried to feed an initial path, generated with SD, to a TIS simulation and run a single cycle with the Qchem interface.

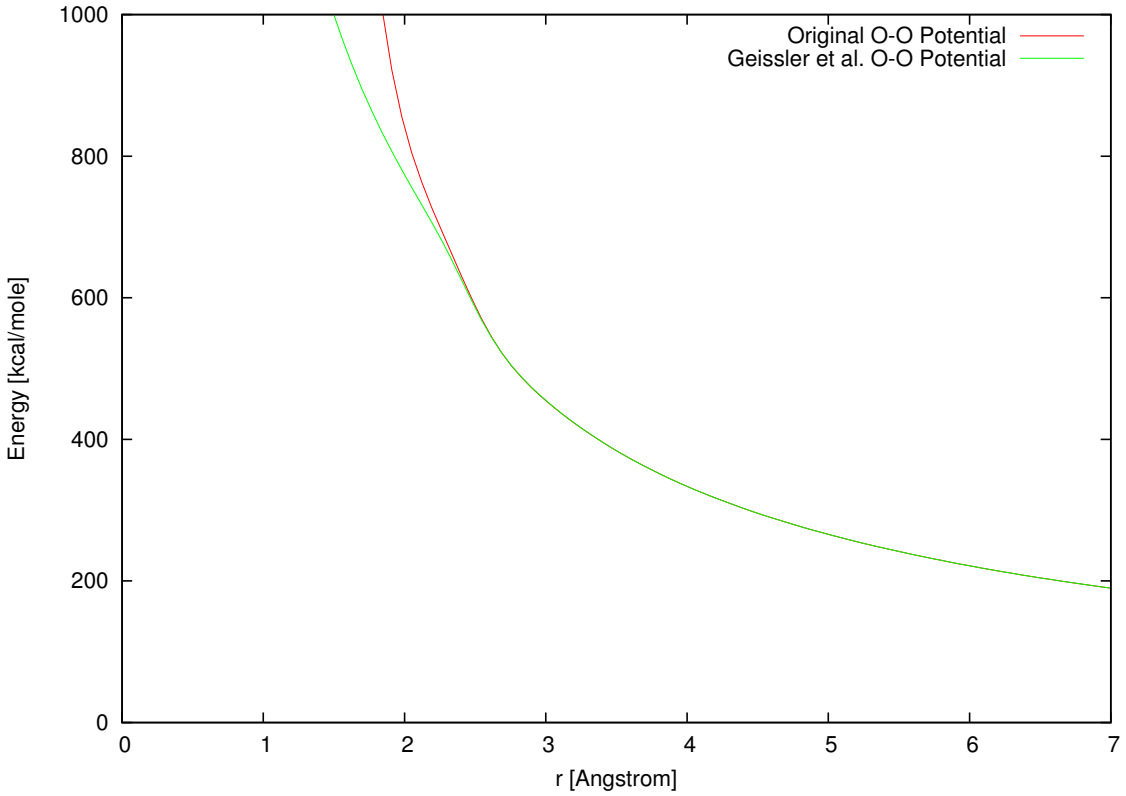


**Figure 4.10:** Top: Plot of the oxygen-oxygen function of potential energy $\phi_{OO}$, Equation 2.2.8 from the article by Stillinger and David (red), and the same potential function from the source code of Geissler et al. (green). For values of $r$ from $\sim 2.45$ and up the difference in potential energy is negligible. When $r \to 0$, $\phi_{OO} \to \infty$. This is true for both functions.

### 4.3.1 Proof of consept by Molecular Dynamics

Running on a cluster using 8×2.6 GHz threads and 16 GB of memory, we managed to complete 1000 steps in 13 hours and 48 minutes. Each step in the cycle did an average of 49 seconds, with variations on how long the convergence of the HF-SCF energy and CC energy took at different steps of the simluation. Configurations of the system that allowed for a quicker convergences of the HF and CCSD energies used less time, for instance. By increasing the number of threads used per calculation, this number could still be reduced, but we chose not to focus on finding this increase in efficiency.

Using the average MD step calculation time as a benchmark for a full RETIS

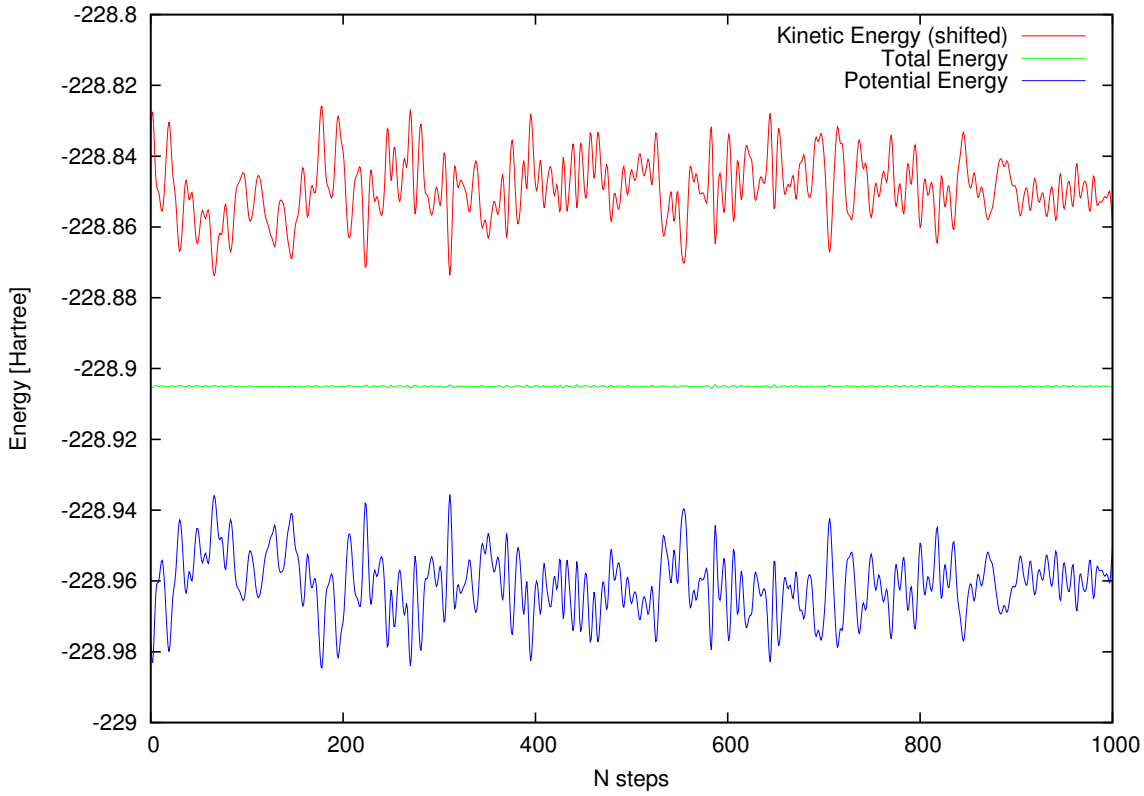


**Figure 4.11:** The potential, kinetic and total energy of a NVE MD simulation using the Qchem CCSD interface, starting at the proposed TS. The kinetic energy illustrated is shifted by a factor equal to the total energy. The total energy is the sum of the potential and (unscaled) kinetic energy, the plot shows energy convergence.

simulation, only using shooting moves, a max pathlength ($\max[\mathcal{T}]$) of 2000 time slices, and with the interfaces as in the Stillinger-David simulation, the *maximum* calculation time of a single cycle on 8×2.6Ghz threads would take

$$49\ \frac{\text{seconds}}{\text{step}} \times 15\ \text{interfaces} \times 2000\ \frac{\max\ \#\text{step}}{\text{interface}} \approx 408\ \text{hours}$$

This would update each path ensemble by generating one new path for each interface, not counting the initialization of each path ensemble, so still way off from a calculation what would yeild a reaction rate. Also, there is no guarantee that the generated path will be a valid one though, as the acceptance criteria have to be fulfilled. Running the simulation on several nodes and perhaps with fewer inter-

faces, in a parallelized RETIS algorithm, could hopefully generate a few acceptable paths which would prove the consept of our work.

### 4.3.2 MD simulation from the transition state

We attempted an MD simulation starting in the proposed transition state, a point where the excess proton is located at an equal distance from its neighbouring oxygens, and where the orderparameter $\Delta\theta$ of the systems configuration is 0. The hope was that we could exploit the symmetry of states $A$ and $B$, so starting two simulations close to this point would yield two halves of a reactive pathway with the QChem inferface. Once two halves were generated, we could plot them together to inspect the path as a whole.

In principle, the results we obtained when running two MD simulations from the TS phase point were the same as 1 TIS or TPS step. We did a successful shooting move from the TS, integrated backwards and forwards in time, and eventually reached the defined stable regions $A$ and $B$. Had this been a TIS simulation, the cycles would have ended once the system crossed into either region. The only difference this path has from an ordinary reactive pathway, is that when the system first crosses the TS going from $A$, all velocities are switched with values picked from a random distribution. So the trajectory shown in Figure 4.12 is not continuous, but as previously shown regarding the order parameter and likelyhood of paths reaching state $B$, such a path could potentially be generated in a TIS/RETIS cycle.

The two simulations each yielded a path going from the TS, one to state $B$ going forwards, and one going to state $A$ going backwards. We knew from the SD TIS/RETIS simulation that the average length of a reactive pathway was somewhere in the vicinity of 400–600 steps, recall from Figure 3.3. The path in Figure 4.12, measured from the crossing of $\Delta\theta = -1.5$ to $\Delta\theta = 1.5$, is approximately 500 steps long. This agrees well with the average path lengths from SD simulations, although this path is not continuous.

Both halves of the path in Figure 4.12 were run for a total of 1000 steps, but only shown with 300 and 400 steps to illustrate the path from $A$ to $B$. The complete backward and forward trajectories are shown in Figure 4.13 and 4.14,

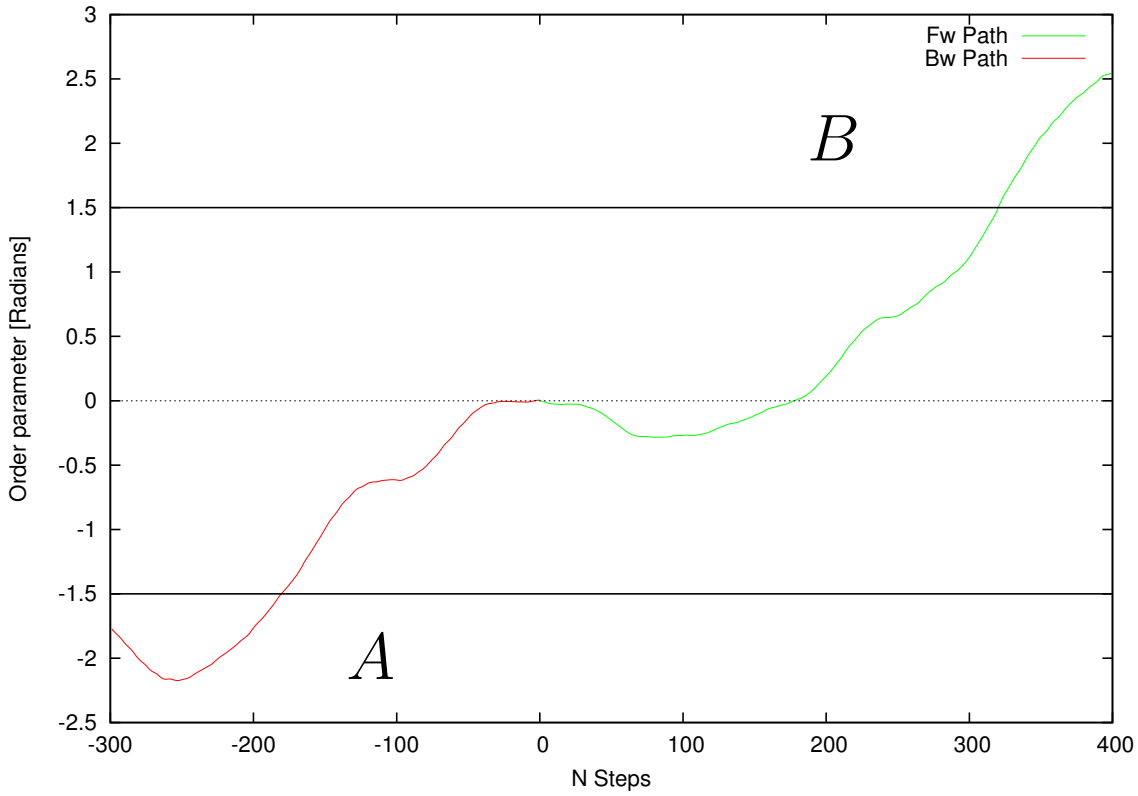


**Figure 4.12:** Order parameter of the system, from a CCMD simulation starting at the proposed TS. The path going backwards (red) to state $A$ is propagating forward in time, but plotted backwards (negative steps on the x-axis) to illustrate the complete path when combined with the forward (green) path. The two solid lines indicate where the regions of $A$ and $B$ would have started if this was a TIS/RETI simulation, and the dashed line indicate the where the system crosses the proposed transition state.

respectively, in red and green. The backward path almost immidiately goes into state $A$, and fluctuates over the interface defining the region. At the very end of the simulation, the system crosses the TS, and from the O1-H7 distance in the lower plot we can see that this point is where the bond breaks and the excess proton is transfered. The forward path from the TS crosses into state $B$, but soon after crosses over TS and into $A$. By observing the bond distance between O1 and H7 we can see that this pathway also behaves like the pathway in Figure 4.1, catalyzing the proton transfer reaction between the stable states. This path is also much shorter, measured from crossing points of $A$ and $B$, than the two combined

trajectories starting from the TS, at about 350–400 steps long.

Figures 4.15 and 4.16 show the potential energy of the two paths. Both figures also include the orderparameter, as to illustrate the transitions of the system and how the potential energy of the system changes with the transitions. The potential energy of the backward path nicely follows the trend of the orderparameter. It shows energy wells, although small and noisy, when the system is close to and within region $A$. At the very end of the backward path, we can observe a possible transition about to occur. The order parameter shows that the system has crossed the TS, the hydrogen distance in Figure 4.13 indicates that the excess proton have been transfered, and the potential energy experiences a drop – all factors indicating that the system should transit into state $B$. The forward path behaves similarly, with a small energy well as the system approches and enters region $B$. The energy between steps 600 and 800 in Figure 4.16 also portrays an energy barrier for the transition reaction, as was shown in Figure 4.4 for the SD potential.

The results show us that it is possible to get a transition when using the specified system and order parameter as in the SD simulations. The computational effort is quite high, with almost 14 hours of calculation time per 1000 steps on 8 threads. The relation of order parameter and O1-H7 distance for states $A$ and $B$ in Figures 4.15 and 4.16 also agrees well with the surface plot from the TIS simulation in Figure 4.5

A shorter simulation could be accomplished, shooting from a point close to the TS to harvest paths. Maybe with the defined regions of $A$ and $B$ closer to the TS than what we have used one would decrease path lengths and computation time, doing the work of Geissler et al. [10] but with a more precise method.

Lastly, a comparison of the potential energy barrier in SD and CC calculations is shown in Figure 4.17. The figure compares the barrier from Figure 4.4 with the transition $B \rightarrow A$ found in the forward trajectory in Figure 4.16 (between N$\approx$500 to N$\approx$850). Plotted against the order parameter $\Delta\theta$, and converted to [kcal/mole]. Both plots have been scaled by a factor, so that minimum energy during their trajectories are zero. The plots show that the potential energy barriers of the two methods are somewhat comparable, with the SD barrier being $\sim 5$ kcal/mole higher than th CC barrier. The CC plot is not accurate, it has been shifted by a rough estimation to fit with the SD plot. It does, however, nicely show the

potential energy barrier from the CC calculation, altough it to is to noisy and uncertain to give an exact activation energy.

### 4.3.3 Simulation by feeding an initial path from SD potential

Additionally, we tried to see if it was possible to harvest some new paths by starting a Coupled-cluster based simulations from generated path ensemble done with the Stillinger-David potential. The limitations of this approach is that we were required to do a successfull simulation with the Stillinger-David potential first, delete all the data except for the last accepted path in each ensemble, and transfer the remaining data to a remote cluster and restart from there. In order to restart properly, we therefore also had to keep every parameter of the calculations done with the Stillinger-David potential. Specifically, we had to keep the maximum allowed path length and the positioning of every interface, in order to restart the simulation. The amount or resources needed to run such a simulation, however, proved to be more than we could possibly set aside of the work, or even have a chance of finishing within submission deadline for this work. Thus, with fewer interfaces, using more threads and/or nodes on the cluster in a parallelized RETIS algorithm, such a simulation is feasible.

By doing fewer cycles of a CC TIS/RETIS scheme, we could still be able to a semi-quantitive path sampling simulation within a reasonable time frame. With our statistical error of 5% after 400000 cycles, we could in theory achieve an error of 100% by only doing 1000 cycles, using a maximum of 420000 hours. The TIS/RETIS scheme could be improved by parallelization of the algorithm. If we imagine seperating the the calculation so that each ensemble use one node, and the threads on that node is used for the CC calculations. This would not be well parallelized, due to two things. Either the path in that ensemble reached the stable states in fewer steps than other ensembles, or that the move used on the ensemble was time reversal or swapping. Regardless, the node would have completed its task before the rest, and would have to wait for the remainder of the TIS/RETIS scheme to finish before attempting a new move. In other words, a parallelization of the TIS/RETIS scheme would be beneficial, but it would not be perfect.

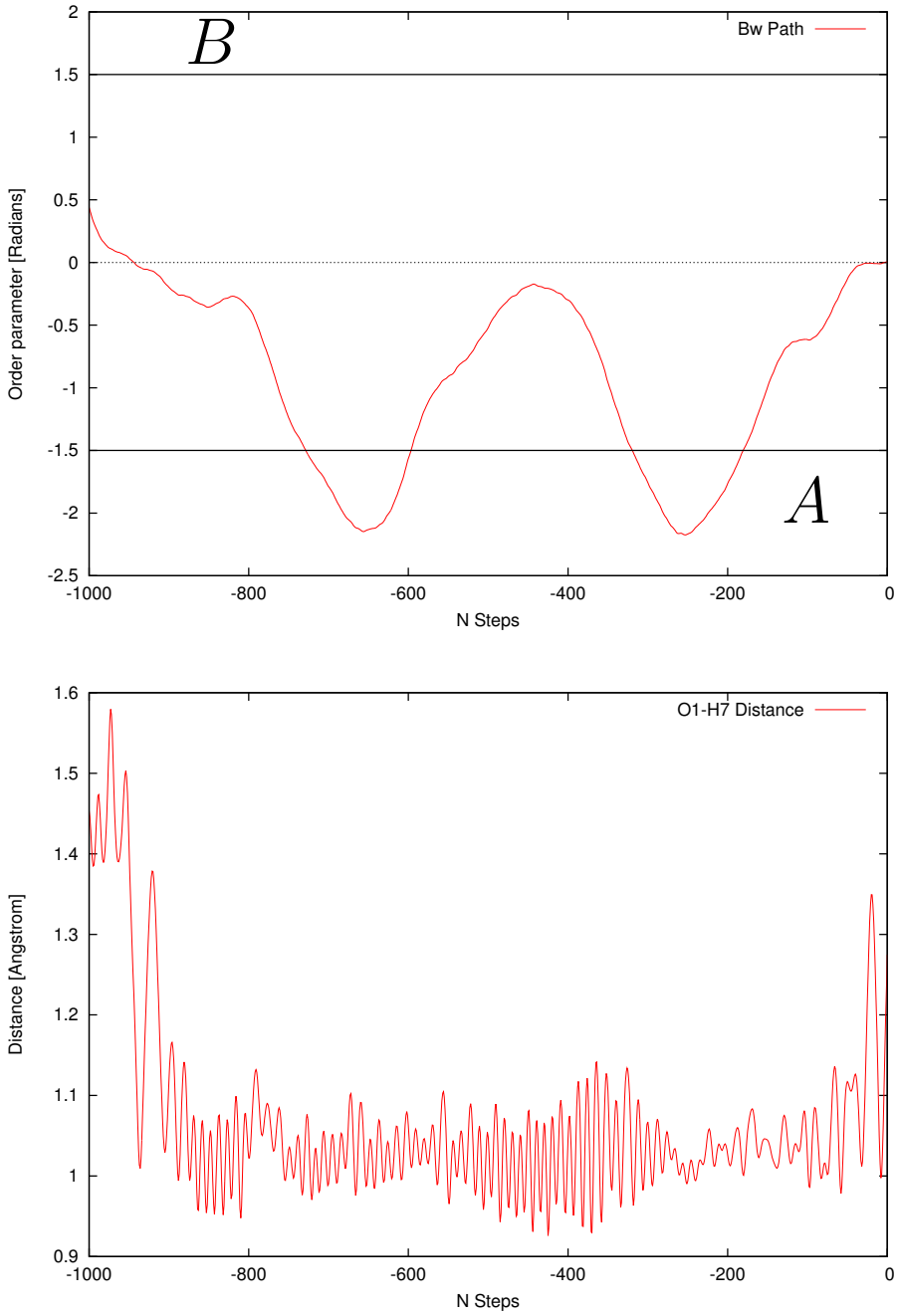


**Figure 4.13:** Order parameter (top) and O1-H7 bond distance (bottom) of the backward trajectory. Even though the system fluctuates over the interface that defines state $A$, the hydrogen stays within 1.1 Å of the oxygen. Solid lines indicate states $A$ and $B$, dashed line indicate region of TS. Plotted with negative values for the steps to indicate going backwards from the TS.

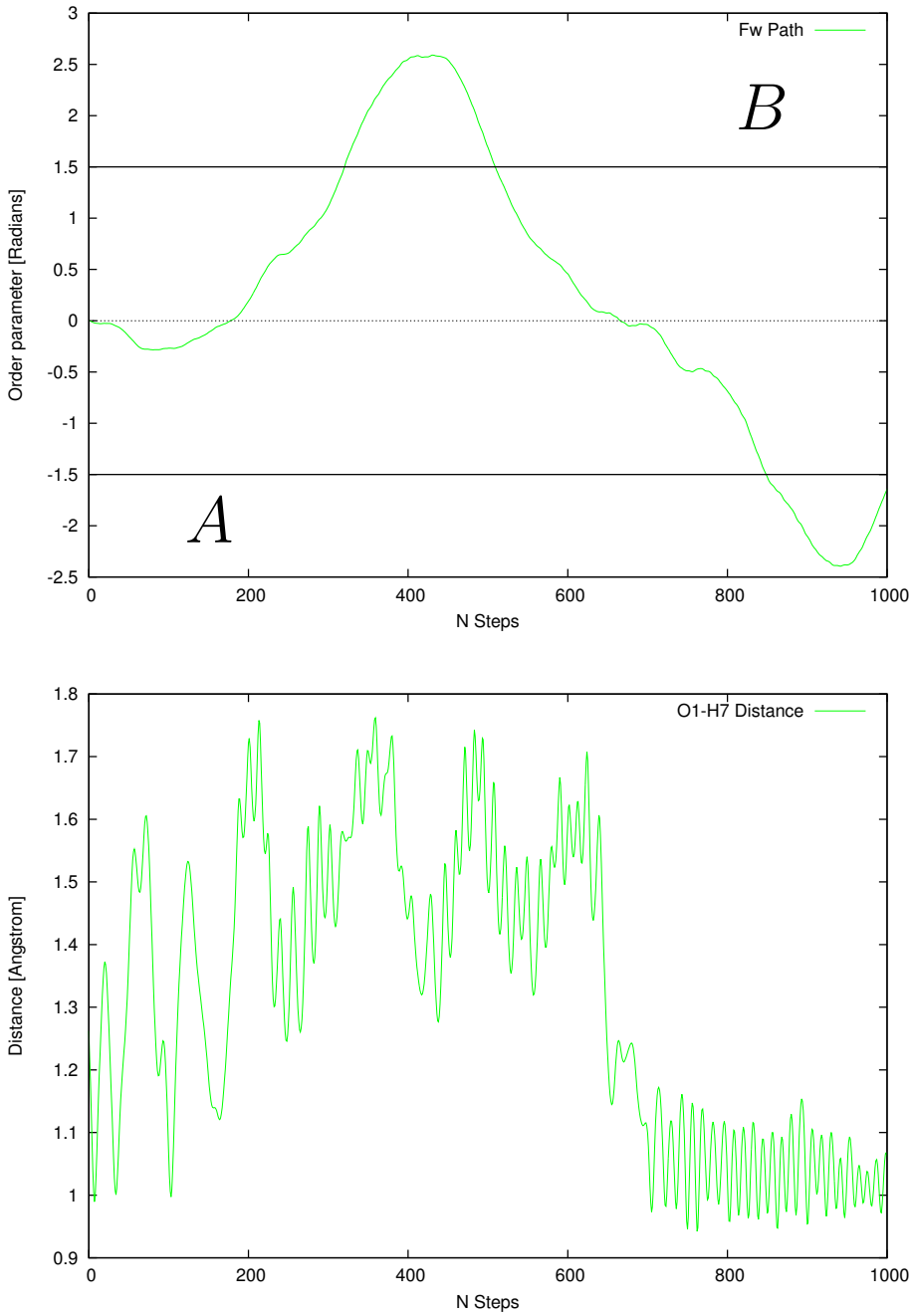


**Figure 4.14:** Order parameter (top) and O1-H7 bond distance (bottom) of the forward trajectory. The system cross into state $B$, and the O1-H7 distance extend to $\sim 1.5$Å, then the system crosses back over TS into $A$, with a O1-H7 distance of $\sim 1$Å. Solid lines indicate states $A$ and $B$, dashed line indicate region of TS.

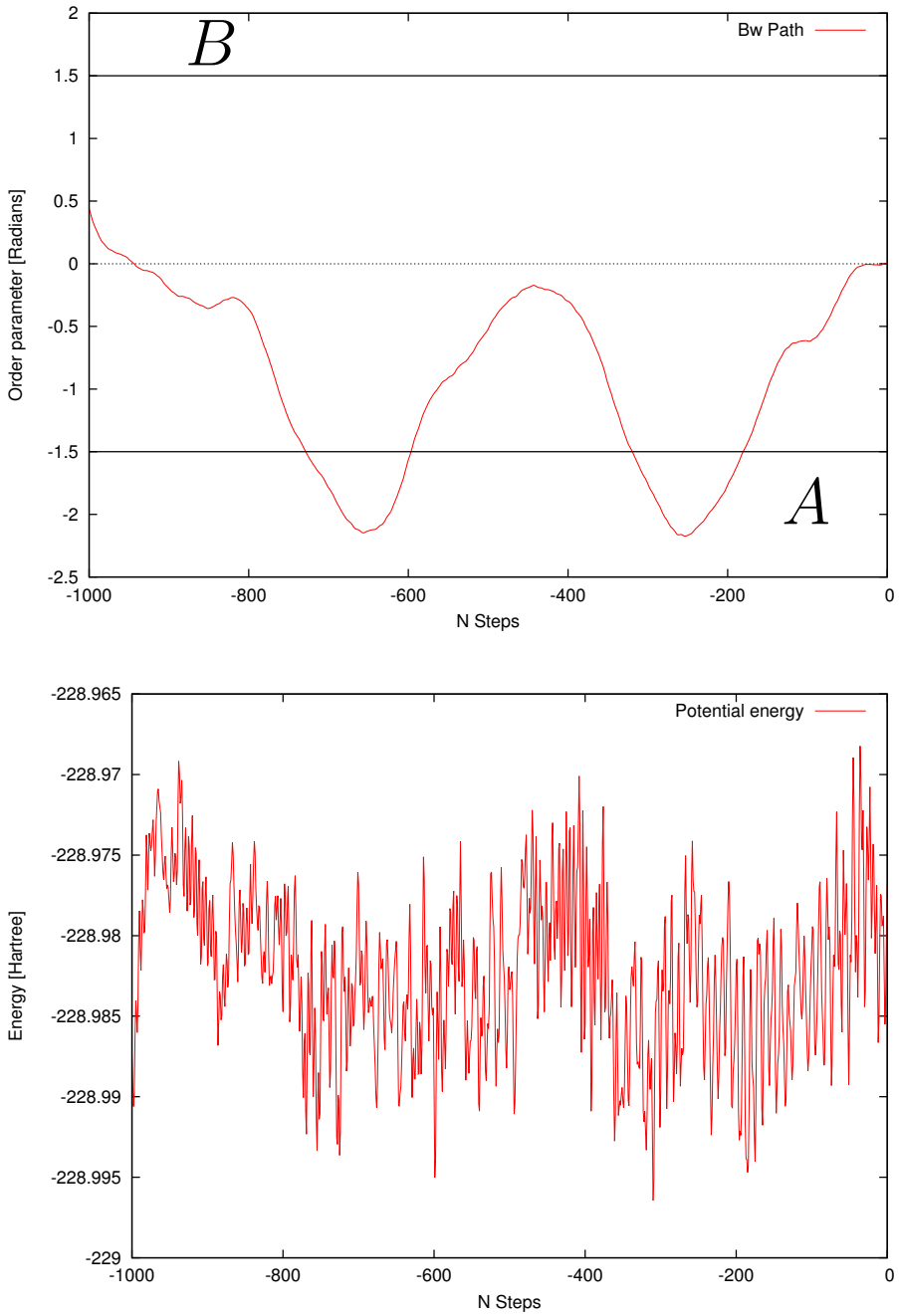


**Figure 4.15:** Order parameter (top) and potential energy (bottom) of the backward trajectory, plotted with negative steps to indicate going backwards from TS. Potential energy decreases as system enters state $A$, and fluctuates as system fluctuates around the interface region.

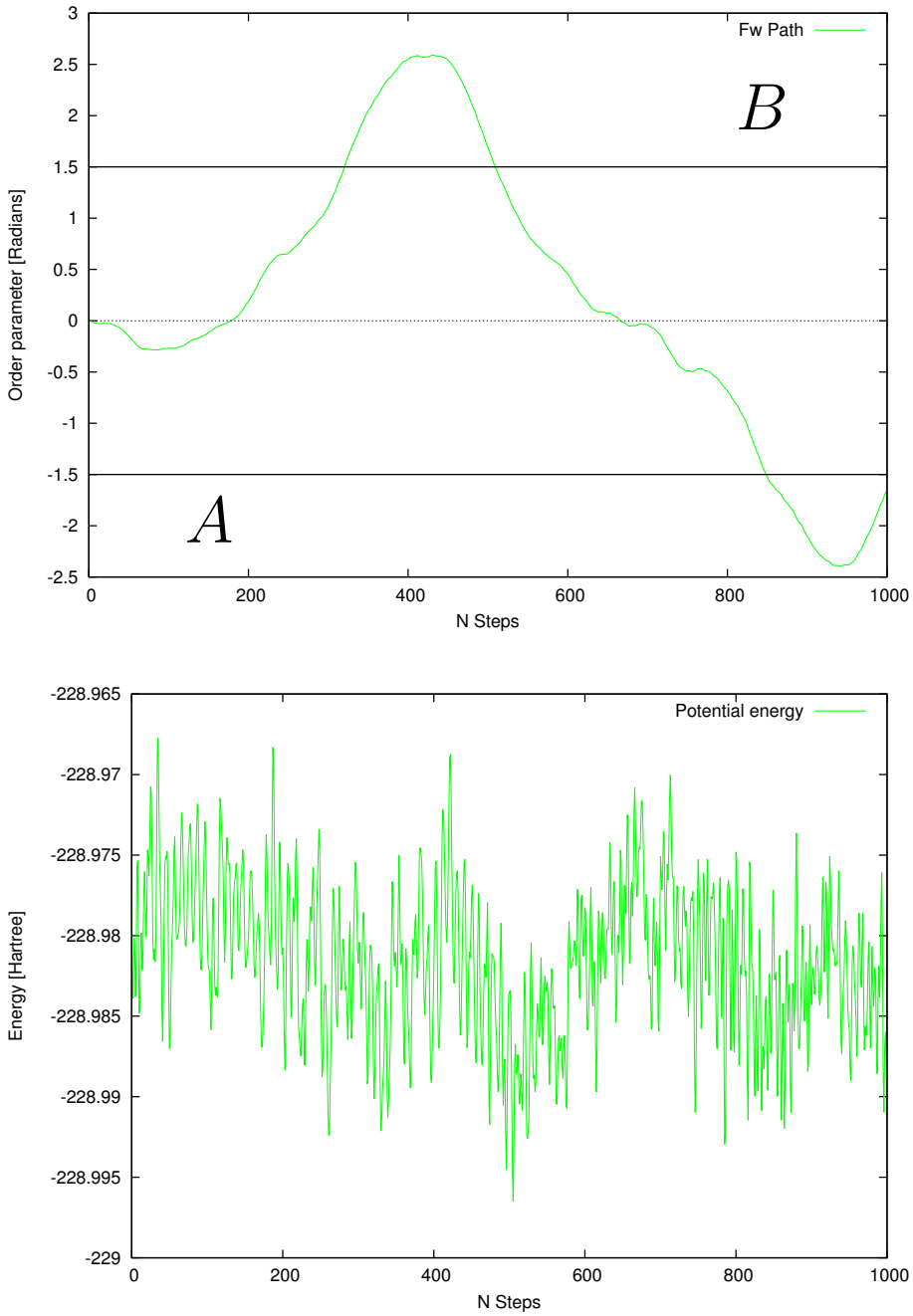


**Figure 4.16:** Order parameter (top) and potential energy (bottom) of the forward trajectory. The potential energy decreases slightly when approaching interface region $B$, with a minimum at approximately 500th step, about to leave region $B$ and cross over TS to $A$, where a small well can be observed as well.

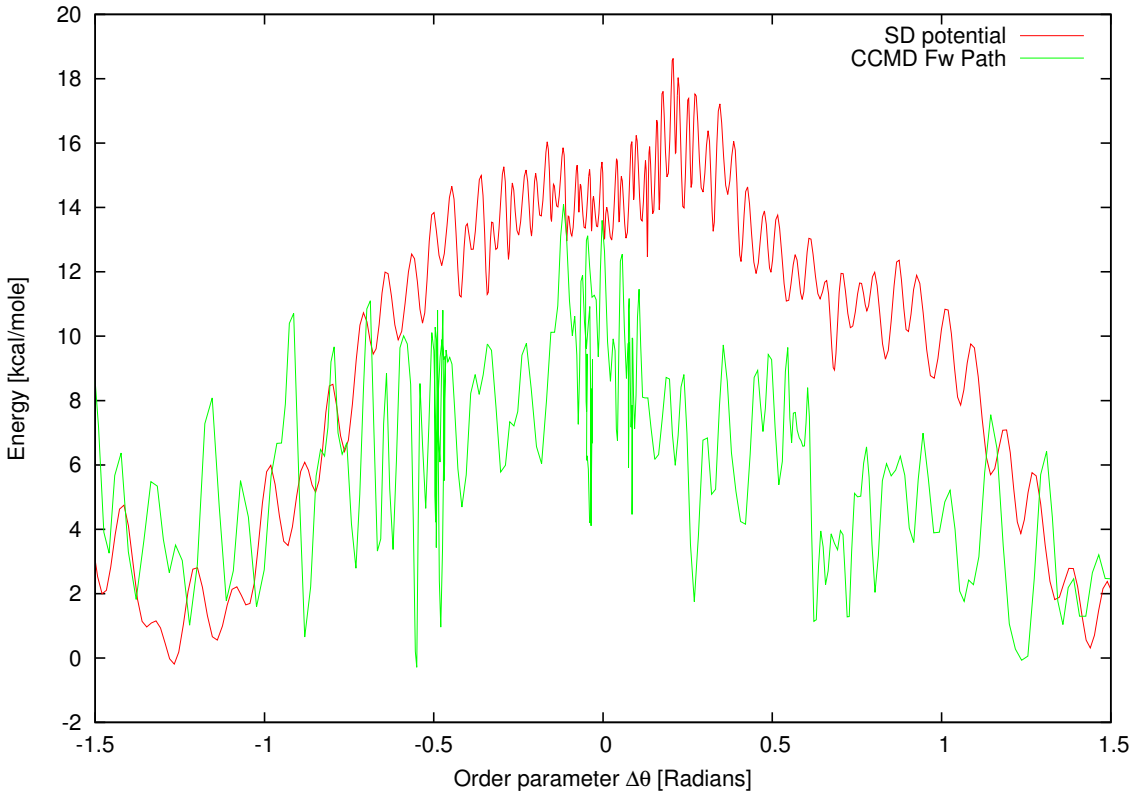


**Figure 4.17:** Comparison of potential energy of transition from Figure 4.16 and potential energy barrier from SD simulation in Figure 4.4. The energy has been scaled from the output of QChem [Hartrees] to [kcal/mole], and both energies have been gauged to zero. The two plots show the energy barrier in between states $A$ and $B$, against the order parameter $\Delta\theta$ of the system. Height of CC potential energy barrier is $\approx 12$ [kcal/mole].

# Chapter 5

# Comments on source code

The end product created for the the Stillinger-David potential and QChem and Cfour interfaces are enclosed in the Appendix.

For both interfacing codes, the goal was to have a routine or function that knew whether the current output from either QChem or CFour was the most recent, since the dynamics required both a single point energy calculation and a read of the output gradient after a truncated geometry optimization. In the CFour interface this was simple, as energy and gradient were stored in separate files that could be removed after reading, and a new calculation would be initiated if the required file was missing. In the QChem interface the energy and gradient were stored in the same file. So when reading the energy for instance, the routine would check if the gradient had been read from the same file, if yes – delete the file. If the energy was the first value read from the file, an empty checkfile was created that the routine would check for when reading the gradient. This solution worked both ways, with a checkfile for both energy and gradient. It is also worth noting that for the (unused) CFour interface, an additional calculation was required in each step, to convert the cartesian coordinates from the dynamics into internal coordinates, and written to a geometry-file with notations on the coordinates that should be used to calculate the gradient in CFour.

In the Stillinger-David potential there were a few limitiations that made our calculations differ from those of Geissler et al. Our dynamics program defines the atomic system with only a total number of particles, not specifying how many

are oxygens. This meant that arrays for the dipoles (equation 2.2.10), and the tensor (equation 2.2.12) contained a lot of zero-values, which required allocation of unnecessary memory. In the tensor $\mathbf{A}$ for instance, the number of non-zero values for the 10 particles in our system was 27 in a total of 900. The dipole arrays were not made global variables either, meaning that the dipole of a previous time step could not be used as initial guess for the self converging iteration in equ. 2.2.10. The result of this was that our iterations of the dipoles maybe used more steps than those of Geissler et al., and individual xyz-components of the dipoles differed by a very small amount, usually about $10^{-8}$. However this is not an issue that changes the results significantly, as the dipole iteration in equ. 2.2.11 is self-converging and will converge towards the same values in both source codes.

# Chapter 6

# Further work

A similar simulation is being studied, where the protonated water-trimer reaction is be studied using DFT based molecular dynamics with a CP2k [36, 37] interface, as opposed to the Stillinger-David potential used in this work. The hope is to get a comparable reaction rate with our work in this thesis. Two new Monte Carlo path sampling moves, named stone-skipping and web-throwing, are also in development by Riccardi and van Erp [38], they help to improve the efficiency of path sampling algorithms by creating sub-trajectories that offer a lower correlation between paths.

With the interfacing between QChem and the TIS/RETIS algorithm, the prospects for further projects using higher and lower level of electron correlation theory are many. As mentioned above, a general improvement to increase the efficiency of the algorithm could be made by using a parallelized TIS/RETIS scheme. This improvement would allow for faster calculations using both the interface with QChem and reactive force fields like the Stillinger-David potential. A parallel RETIS scheme in combination with the power of QChem could be used to simulate the protonated water-trimer with fewer cycles, within reasonable timeframes. Development of multi-level Coupled-cluster theory by Myhre et al. [39] could also improve on further simulations, allowing for separation of the molecular system across chemical bonds. With different levels of theory applied to strongly and weakly interacting electron pairs, the theory streamlines the electron correlation calculations, reducing the overall computation time requirement.

# Chapter 7

# Conclusion

The aim of this study was to combine the power of electron correlation with the flexibility of path and interface sampling techniques, on a protonated water trimer system. This system would also be studied with the Stillinger-David potential in order to calculate a rate of reaction for the catalyzed proton transfer, comparable to the work by Geissler et al. [9].

We simulated transitions in the protonated water trimer using both TIS and RETIS schemes at 300 Kelvin in order to calculate the rate of reaction. Our simulations gave two rates, one using TIS at $3.8168 \cdot 10^3 s^{-1}$, and one using RETIS at $4.61742 \cdot 10^3 s^{-1}$. The results are lower than the rates reported in litterature based on DFT but agree with the statement of Geissler et al. who studied the reaction using both DFT [] and using SD []. The actuall rate of the SD simulations is, however, unclear since it is no explicitly reported. When we tried to estimate the rate from the slope of the correlation function in Ref. 9, it seemed that the result is even lower, by a few orders of magnitude, than our SD result. We can, however, not exclude that there has been an error in the figure such as wrong units or conversion factor.

We successfully created an interface between a dynamics program TISMOL and two quantum chemistry programs, CFour and QChem. With the QChem interface we were able to simulate two halves of a complete trajectory, generating a pathway by combining the two halves. Using this interface to compute energies and forces using coupled-cluster is feasable, but will take considerable time to preform, with

almost 14 hours of calculation time for 1000 time steps. A full TIS simulation would scale with the number of interfaces as well, and repeating the setup used in the SD simulations for 1000 cycles gives a maximum estimate required time of 420000 hours on 8 threads.

# Bibliography


[1] Aneesur Rahman and Frank H Stillinger.
Molecular dynamics study of liquid water.
*The Journal of Chemical Physics*, 55(7):3336–3359, 1971.

[2] William L Jorgensen, Jayaraman Chandrasekhar, Jeffry D Madura, Roger W Impey, and Michael L Klein.
Comparison of simple potential functions for simulating liquid water.
*The Journal of chemical physics*, 79(2):926–935, 1983.

[3] H Kistenmacher, GC Lie, H Popkie, and E Clementi.
Study of the structure of molecular complexes. vi. dimers and small clusters of water molecules in the hartree-fock approximation.
*The Journal of Chemical Physics*, 61(2):546–561, 1974.

[4] V Ya Antonchenko, AS Davidov, and VV Ilyin.
Physics of water (in Russian).
*Naukova Dumka, Kiev*, 1986.

[5] Frank H Stillinger and Carl W David.
Polarization model for water and its ionic dissociation products.
*The Journal of Chemical Physics*, 69(4):1473–1484, 1978.

[6] V Ya Antonchenko, AS Davydov, and VV Il'in.
Fundamentals of the physics of water (in Russian).
*Naukova Dumka, Kiev*, 1991.

[7] Frank H Stillinger and Carl W David.

Study of the water octamer using the polarization model of molecular interactions.
*The Journal of Chemical Physics*, 73(7):3384–3389, 1980.

[8] David S Eisenberg, Walter Kauzmann, et al.
*The structure and properties of water*, volume 123.
Clarendon Press Oxford.

[9] Philip L Geissler, C Dellago, and D Chandler.
Chemical dynamics of the protonated water trimer analyzed by transition path sampling.
*Physical Chemistry Chemical Physics*, 1(6):1317–1322, 1999.

[10] Phillip L Geissler, Christoph Dellago, David Chandler, Jürg Hutter, and Michele Parrinello.
Ab initio analysis of proton transfer dynamics in $[(H_2O)_3H]^+$: comparison of density functional theory and wavefunction-based methods.
*Chemical Physics Letters*, 321(3):225–230, 2000.

[11] Phillip L Geissler, Troy Van Voorhis, and Christoph Dellago.
Potential energy landscape for proton transfer in $(H_2O)_3H^+$: comparison of density functional theory and wavefunction-based methods.
*Chemical Physics Letters*, 324(1):149–155, 2000.

[12] Titus S van Erp.
Reaction rate calculation by parallel path swapping.
*Physical Review Letters*, 98(26):268301, 2007.

[13] Attila Szabo and Neil S Ostlund.
*Modern quantum chemistry: introduction to advanced electronic structure theory.*
Courier Corporation, 1989.

[14] Peter W Atkins and Ronald S Friedman.
*Molecular quantum mechanics.*
Oxford university press, 5th edition, 2011.

[15] Clemens Carel Johannes Roothaan.
New developments in molecular orbital theory.
*Reviews of modern physics*, 23(2):69, 1951.

[16] Chr Møller and Milton S Plesset.
Note on an approximation treatment for many-electron systems.
*Physical Review*, 46(7):618, 1934.

[17] Thomas A Weber and Frank H Stillinger.
Reactive collisions of hydronium and hydroxide ions studied with the polarization model.
*The Journal of Physical Chemistry*, 86(8):1314–1318, 1982.

[18] Igor Zhyganiuk.
Generalized Stillinger–David potential.
*arXiv preprint arXiv:1202.4491*, 2012.

[19] Daan Frenkel and Berend Smit.
*Understanding molecular simulation: from algorithms to applications*.
Academic press, 2 edition, 2002.

[20] E Wigner.
The transition state method.
*Transactions of the Faraday Society*, 34:29–41, 1938.

[21] Titus S van Erp.
Dynamical rare event simulation techniques for equilibrium and nonequilibrium systems.
*Advances in Chemical Physics*, 151:27, 2012.

[22] Christoph Dellago, Peter Bolhuis, and Phillip L Geissler.
Transition path sampling.
*Advances in chemical physics*, 123:1–78, 2002.

[23] Christoph Dellago, Peter G Bolhuis, and Phillip L Geissler.
Transition path sampling methods.

*Computer Simulations in Condensed Matter Systems: From Materials to Chemical Biology Volume 1*, pages 349–391, 2006.

[24] Peter G Bolhuis, David Chandler, Christoph Dellago, and Phillip L Geissler.
Transition path sampling: Throwing ropes over rough mountain passes, in the dark.
*Annual review of physical chemistry*, 53(1):291–318, 2002.

[25] Titus S van Erp, Daniele Moroni, and Peter G Bolhuis.
A novel path sampling method for the calculation of rate constants.
*The Journal of Chemical hysics*, 118(17):7762–7774, 2003.

[26] Christoph Dellago, Peter G Bolhuis, Félix S Csajka, and David Chandler.
Transition path sampling and the calculation of rate constants.
*The Journal of chemical physics*, 108(5):1964–1977, 1998.

[27] Titus S van Erp.
Efficiency analysis of reaction rate calculation methods using analytical models I: The two-dimensional sharp barrier.
*The Journal of chemical physics*, 125(17):174106, 2006.

[28] Christoph Dellago, Peter G Bolhuis, and David Chandler.
On the calculation of reaction rate constants in the transition path ensemble.
*The Journal of chemical physics*, 110(14):6617–6625, 1999.

[29] Titus S van Erp.
Efficient path sampling on multiple reaction channels.
*Computer physics communications*, 179(1):34–40, 2008.

[30] Jing Kong, Christopher A White, Anna I Krylov, David Sherrill, Ross D Adamson, Thomas R Furlani, Michael S Lee, Aaron M Lee, Steven R Gwaltney, Terry R Adams, et al.
Q-chem 2.0: a high-performance ab initio electronic structure program package.
*Journal of Computational Chemistry*, 21(16):1532–1548, 2000.

[31] Yihan Shao, Laszlo Fusti Molnar, Yousung Jung, Jörg Kussmann, Christian Ochsenfeld, Shawn T Brown, Andrew TB Gilbert, Lyudmila V Slipchenko, Sergey V Levchenko, Darragh P O'Neill, et al.
Advances in methods and algorithms in a modern quantum chemistry program package.
*Physical Chemistry Chemical Physics*, 8(27):3172–3191, 2006.

[32] Yihan Shao, Zhengting Gan, Evgeny Epifanovsky, Andrew TB Gilbert, Michael Wormit, Joerg Kussmann, Adrian W Lange, Andrew Behn, Jia Deng, Xintian Feng, et al.
Advances in molecular quantum chemistry contained in the Q-Chem 4 program package.
*Molecular Physics*, 113(2):184–215, 2015.

[33] Quantum computational software, molecular modelling, visualization.
URL `http://www.q-chem.com`.

[34] Cfour.
URL `http://www.cfour.de`.

[35] The NOTUR-cluster Stallo.
URL `http://www.notur.no/hardware/stallo/`.

[36] A CP2k.
General program to perform molecular dynamics simulations.
*CP2k developers group under the terms of the GNU General Public License.*

[37] CJ Mundy, F Mohamed, F Schiffman, G Tabacchi, H Forbert, W Kuo, J Hutter, M Krack, M Iannuzzi, M McGrath, et al.
Cp2k software package.
*There is no corresponding record for this reference*, 2000.

[38] E Riccardi and T van Erp.
Stone Skipping and Web Throwing: Efficient Monte Carlo moves in trajectory space.
unpublished article, 2016.

[39] Rolf H Myhre, Alfredo MJ Sánchez de Merás, and Henrik Koch.
Multi-level Coupled-Cluster theory.
*The Journal of chemical physics*, 141(22):224105, 2014.

# Appendices

# Appendix A

# Stillinger-David force equations

Similarly to Equation (2.2.10), a dipole field array is calculated by

$$\vec{\nu}_i^{(0)} = \sum_{\substack{j=1,\\ j\neq i}}^{N} -\alpha * e_j * \frac{1 - L_O(r_{ij})}{r_{ij}^3} * \vec{r}_{ij} \tag{A.1}$$

also with the same iteration scheme as Equation (2.2.11)

$$\vec{\nu}_i^{(n+1)} = \sum_{j=1}^{N_o} \mathbf{A}(\vec{r}_{ij}) \cdot \vec{\nu}_i^{(n)} \tag{A.2}$$

This array will be used by the oxygen-hydrogen and oxygen-oxygen terms below.

The force functions are derived from the total potential function $\Phi_{total}$ (2.2.1)

$$\vec{F}_{total} = \vec{F}_{(1)} + \vec{F}_{(2)} = \frac{d}{dr}\Phi_{total} \tag{A.3}$$

where $\vec{F}_{(1)}$ is the derivative of the Coulombic potential functions (Equation 2.2.6–2.2.8), and $\vec{F}_{(2)}$ is the derivative of the dipole interaction potential.

$$\vec{F}_{(2)}(i) = \sum_{\substack{j=1,\\ j\neq i}}^{N_o} \vec{f}_{OO}^{(2)}(\vec{r}_{ij}) + \sum_{\substack{l=1,\\ l\neq i}}^{N_H} \vec{f}_{OH}^{(2)}(\vec{r}_{ij}) \tag{A.4}$$

Since the $F_{(2)}$-term depends on dipole moments, there is no term for H-H interactions, these are only calculated with Coulomb forces. The function for the force from oxygen-hydrogen interactions becomes

$$\vec{f}^{(2)}_{OH}(\vec{r}_{ij}) = \frac{1}{2}\sum_{j=1}^{N_H} e_j(sL(r_{ij})*\vec{\mu}_i + sK(r_{ij})*\vec{\nu}_i + \frac{(\vec{\mu}_i\cdot\vec{r}_{ij})dL(r_{ij}) + (\vec{\nu}_i\cdot\vec{r}_{ij})dK(r_{ij})}{r_{ij}} * \vec{r}_{ij}) \tag{A.5}$$

And the oxygen-oxygen part of the force formula is

$$\begin{aligned}
\vec{f}^{(2)}_{OO}(\vec{r}_{ij}) = &-\frac{1}{2}\sum_{\substack{j=1,\\ j\neq i}}^{N_O} e_j\left((\vec{\mu}_j-\vec{\mu}_i)sL(r_{ij}) + ((\vec{\mu}_j\cdot\vec{r}_{ij}) - (\vec{\mu}_i\cdot\vec{r}_{ij}))\frac{dL(r_{ij})}{r_{ij}}\right)\\
&+ e_j\left((\vec{\nu}_j-\vec{\nu}_i)sK(r_{ij}) + ((\vec{\nu}_j\cdot\vec{r}_{ij}) - (\vec{\nu}_i\cdot\vec{r}_{ij}))\frac{dK(r_{ij})}{r_{ij}}\right)\\
&- \frac{3sK(r_{ij})}{r_{ij}^4}\left((\vec{\nu}_j*(\vec{\mu}_i\cdot\vec{r}_{ij}) + \vec{\mu}_i*(\vec{\nu}_j\cdot\vec{r}_{ij}))\,r_{ij}^2 - 2(\vec{\nu}_j\cdot\vec{r}_{ij})(\vec{\mu}_i\cdot\vec{r}_{ij})\vec{r}_{ij}\right)\\
&- \frac{3sK(r_{ij})}{r_{ij}^4}\left((\vec{\nu}_i*(\vec{\mu}_j\cdot\vec{r}_{ij}) + \vec{\mu}_j*(\vec{\nu}_i\cdot\vec{r}_{ij}))\,r_{ij}^2 - 2(\vec{\nu}_i\cdot\vec{r}_{ij})(\vec{\mu}_j\cdot\vec{r}_{ij})\vec{r}_{ij}\right)\\
&+ \left((\vec{\nu}_j\cdot\vec{\mu}_i) + (\vec{\nu}_i\cdot\vec{\mu}_j) - \frac{3}{r_{ij}^2}\left[(\vec{\nu}_i\cdot\vec{r}_{ij})(\vec{\mu}_j\cdot\vec{r}_{ij}) + (\vec{\mu}_j\cdot\vec{r}_{ij})(\vec{\nu}_i\cdot\vec{r}_{ij})\right]\right)\frac{dK(r_{ij})}{r_{ij}}\vec{r}_{ij}
\end{aligned} \tag{A.6}$$

using the screening functions, and derivatives of screening functions, defined as

$$sL(r_{ij}) = \frac{1 - L_O(r_{ij})}{r_{ij}^3} \tag{A.7}$$

$$sK(r_{ij}) = \frac{1 - K_O(r_{ij})}{r_{ij}^3} \tag{A.8}$$

$$dL(r_{ij}) = \frac{\frac{d}{dr_{ij}}(1 - L_O(r_{ij}))}{r_{ij}^3} - 3\frac{(1 - L_O(r_{ij}))}{r_{ij}} \tag{A.9}$$

$$dK(r_{ij}) = \frac{\frac{d}{dr_{ij}}(1 - K_O(r_{ij}))}{r_{ij}^3} - 3\frac{(1 - K_O(r_{ij}))}{r_{ij}} \tag{A.10}$$

# Appendix B

# Stillinger-David simulation parameters

| | | Sampling move frequency | | |
|---|---|---|---|---|
| Interface $i$ | $\lambda_i$ | Shooting | Time-reversal | Swapping |
| A | -1.50 | 100% | 0% | 0% |
| 1 | -1.20 | 100% | 0% | 0% |
| 2 | -1.00 | 100% | 0% | 0% |
| 3 | -0.90 | 100% | 0% | 0% |
| 4 | -0.80 | 100% | 0% | 0% |
| 5 | -0.70 | 100% | 0% | 0% |
| 6 | -0.60 | 100% | 0% | 0% |
| 7 | -0.55 | 100% | 0% | 0% |
| 8 | -0.50 | 100% | 0% | 0% |
| 9 | -0.45 | 100% | 0% | 0% |
| 10 | -0.40 | 100% | 0% | 0% |
| 11 | -0.35 | 100% | 0% | 0% |
| 12 | -0.30 | 100% | 0% | 0% |
| 13 | -0.25 | 100% | 0% | 0% |
| 14 | -0.10 | 100% | 0% | 0% |
| B | 1.50 | 100% | 0% | 0% |

**Table B.1:** Table of the interfaces used in the Stillinger-David TIS simulation. The orderparameter $\lambda(x_i)$ value of the interface/surface, and the frequencies of the different path generation moves for the different ensembles.

| | | Sampling move frequency | | |
|---|---|---|---|---|
| Interface $i$ | $\lambda_i$ | Shooting | Time-reversal | Swapping |
| A | -1.50 | 50% | 25% | 25% |
| 1 | -1.20 | 50% | 25% | 25% |
| 2 | -1.00 | 50% | 25% | 25% |
| 3 | -0.90 | 50% | 25% | 25% |
| 4 | -0.80 | 50% | 25% | 25% |
| 5 | -0.70 | 50% | 25% | 25% |
| 6 | -0.60 | 50% | 25% | 25% |
| 7 | -0.55 | 50% | 25% | 25% |
| 8 | -0.50 | 50% | 25% | 25% |
| 9 | -0.45 | 50% | 25% | 25% |
| 10 | -0.40 | 50% | 25% | 25% |
| 11 | -0.35 | 50% | 25% | 25% |
| 12 | -0.30 | 50% | 25% | 25% |
| 13 | -0.25 | 50% | 25% | 25% |
| 14 | -0.10 | 50% | 25% | 25% |
| B | 1.50 | 50% | 25% | 25% |

**Table B.2:** Table of the interfaces used in the Stillinger-David RETIS simulation. The orderparameter $\lambda(x_i)$ value of the interface/surface, and the frequencies of the different path generation moves for the different ensembles.

# Appendix C

# Crossing probabilities from Stillinger-David simulations

| | | Crossing probability | |
|---|---|---|---|
| $P(\lambda_{i+1}\|\lambda_i)$ | $\lambda_i$ | Value | Error (%) |
| $P(\lambda_1\|\lambda_A)$ | -1.50 | 0.530477 | 0.395717 |
| $P(\lambda_2\|\lambda_1)$ | -1.20 | 0.209959 | 0.572496 |
| $P(\lambda_3\|\lambda_2)$ | -1.00 | 0.275744 | 0.677078 |
| $P(\lambda_4\|\lambda_3)$ | -0.90 | 0.190232 | 0.982545 |
| $P(\lambda_5\|\lambda_4)$ | -0.80 | 0.128382 | 1.336293 |
| $P(\lambda_6\|\lambda_5)$ | -0.70 | 0.088660 | 1.711813 |
| $P(\lambda_7\|\lambda_6)$ | -0.60 | 0.260006 | 1.117660 |
| $P(\lambda_8\|\lambda_7)$ | -0.55 | 0.240136 | 1.190029 |
| $P(\lambda_9\|\lambda_8)$ | -0.50 | 0.236366 | 1.221509 |
| $P(\lambda_{10}\|\lambda_9)$ | -0.45 | 0.245834 | 1.228654 |
| $P(\lambda_{11}\|\lambda_{10})$ | -0.40 | 0.260451 | 1.191842 |
| $P(\lambda_{12}\|\lambda_{11})$ | -0.35 | 0.302876 | 1.832600 |
| $P(\lambda_{13}\|\lambda_{12})$ | -0.30 | 0.375111 | 1.668620 |
| $P(\lambda_{14}\|\lambda_{13})$ | -0.25 | 0.230849 | 2.959962 |
| $P(\lambda_B\|\lambda_{14})$ | -0.10 | 0.718324 | 1.010867 |

**Table C.1:** Table of interface crossing probabilites from the SD TIS simulation, with the corresponding calculated error of the particular interface, $i$, crossing. Note that for interface $i = 14$, the crossing probability $P(\lambda_{i+1}|\lambda_i) = P(\lambda_{\mathcal{B}}|\lambda_{14})$, meaning the probability of paths reaching region $\mathcal{B}$ after crossing $\lambda(x) = \lambda_{14}$. Errors was calculated using block averaging.

| | | Crossing probability | |
|---|---|---|---|
| $P(\lambda_{i+1}\|\lambda_i)$ | $\lambda_i$ | Value | Error (%) |
| $P(\lambda_1\|\lambda_A)$ | -1.50 | 0.530714 | 0.365688 |
| $P(\lambda_2\|\lambda_1)$ | -1.20 | 0.206104 | 0.720709 |
| $P(\lambda_3\|\lambda_2)$ | -1.00 | 0.275152 | 0.851287 |
| $P(\lambda_4\|\lambda_3)$ | -0.90 | 0.193877 | 1.167668 |
| $P(\lambda_5\|\lambda_4)$ | -0.80 | 0.130012 | 1.623652 |
| $P(\lambda_6\|\lambda_5)$ | -0.70 | 0.088485 | 2.168514 |
| $P(\lambda_7\|\lambda_6)$ | -0.60 | 0.257944 | 1.338816 |
| $P(\lambda_8\|\lambda_7)$ | -0.55 | 0.244664 | 1.339061 |
| $P(\lambda_9\|\lambda_8)$ | -0.50 | 0.234729 | 1.392142 |
| $P(\lambda_{10}\|\lambda_9)$ | -0.45 | 0.236927 | 1.423942 |
| $P(\lambda_{11}\|\lambda_{10})$ | -0.40 | 0.256507 | 1.351922 |
| $P(\lambda_{12}\|\lambda_{11})$ | -0.35 | 0.307262 | 1.546441 |
| $P(\lambda_{13}\|\lambda_{12})$ | -0.30 | 0.384142 | 1.672591 |
| $P(\lambda_{14}\|\lambda_{13})$ | -0.25 | 0.266024 | 4.236304 |
| $P(\lambda_B\|\lambda_{14})$ | -0.10 | 0.753523 | 1.933681 |

**Table C.2:** Table of interface crossing probabilites from the SD RETIS simulation, with the corresponding calculated error of the particular interface crossing. Note that for interface $i = 14$, the crossing probability $P(\lambda_{i+1}|\lambda_i) = P(\lambda_{\mathcal{B}}|\lambda_{14})$, meaning probability of paths reaching region $\mathcal{B}$ after crossing $\lambda(x) = \lambda_{14}$. Errors was calculated using block averaging.

# Appendix D

# Stillinger-David potential source code

# Appendix E

# QChem and CFour interfacing source code